Chapter 2
Cavitation Mapping

Ting Ding, Hui Yin, Hong Hu, Chen Bai and Mingxi Wan

Keywords High-speed photography · Sonoluminescence · Sonochemiluminescence · Active cavitation mapping · Passive cavitation mapping · Precise spatial–temporal mapping · Ultrafast mapping · Doppler method

2.1 Introduction

When the acoustic pressure of ultrasound propagating in a medium is higher than a threshold value, one or more gas pockets (bubbles) can form Apfel (1984). During ultrasound exposure, these gas bubbles may grow, oscillate, and collapse, during which they are called "active" cavitation bubbles. When ultrasound exposure is turned off, some active cavitation bubbles tend to dissolve, leaving only the remaining "residual" cavitation bubbles. Particularly with pulsed ultrasound, residual cavitation bubbles between successive ultrasound exposures may act as cavitation nuclei to enhance cavitation effects. As cavitation plays important roles in almost all ultrasound applications—such as tumor ablation (Kennedy 2005), lithotripsy (Coleman et al. 1987), and hemostasis (Vaezy et al. 1999)—a better

T. Ding · H. Yin · H. Hu · C. Bai · M. Wan (✉)
The Key Laboratory of Biomedical Information Engineering of Ministry of Education, Department of Biomedical Engineering, School of Life Science and Technology, Xi'an Jiaotong University, 710049 Xi'an, People's Republic of China
e-mail: mxwan@mail.xjtu.edu.cn

T. Ding
e-mail: dtingb@gmail.com

H. Yin
e-mail: yhlovegxm@gmail.com

H. Hu
e-mail: huqianqin18@163.com

C. Bai
e-mail: baichen1986@gmail.com

M. Wan et al. (eds.), *Cavitation in Biomedicine*,
DOI 10.1007/978-94-017-7255-6_2

understanding of the spatial–temporal distribution of cavitation bubbles is essential to optimize these applications. For decades, techniques for detecting and mapping cavitation have been developed, and these techniques mainly include optical and acoustic methods (Barnett 1998).

Optical methods, such as high-speed photography, sonoluminescence (SL), and sonochemiluminescence (SCL), can directly visualize the spatial distribution of cavitation bubbles with time, but they can only be used in transparent media. High-speed photography can be employed to capture images of bubble dynamics and distribution when ultrasound exposure is on, and this powerful tool has a sufficiently high frame rate. Its time resolution can reach the nanosecond level, and its spatial resolution can be improved by combining it with microscopes, for example, an inverted microscope or a long-distance microscope. However, compared to high-speed photography, SL and SCL can provide more information about the spatial distribution of chemically active cavitation bubbles.

The acoustic methods commonly used to detect cavitation include active cavitation detection (ACD), passive cavitation detection (PCD), and the Doppler method. In general, ACD is a pulse-echo system based on the scattered acoustic signals from bubbles, and it is sufficient to monitor the existence and dissolution of bubbles. ACD using a focused transducer with a high center frequency is more sensitive to single bubbles in the micron size range. Nevertheless, ACD can only be used when ultrasound exposure is turned off otherwise it might interfere with the interrogating pulse. Conversely, PCD has been used extensively to monitor cavitation activity during ultrasound exposure, where it passively records acoustic emissions from cavitating bubbles. Compared with ACD, PCD is generally more sensitive to either resonance-sized bubbles or clouds of bubbles. ACD and PCD are the classic methods for detecting acoustic cavitation. These have been applied not only in water, but also in tissue. However, both of these acoustic techniques are one-dimensional detection methods, and thus, they cannot reflect the spatial distribution of cavitation. The Doppler method, however, can obtain a much higher frequency shift range that caused by translation motion of a solid particle, so it can effectively distinguish a cavitation event.

Recently, ACD and PCD have been adapted to cavitation mapping techniques, specifically active cavitation mapping (ACM) and passive cavitation mapping (PCM). For these techniques, a linear array is connected to the ultrasound system to increase the spatial coverage of cavitation detection. In this chapter, we introduce two ACM methods: precise active cavitation mapping (PACM) that uses a modified ultrasound line-by-line scanning and ultrafast active cavitation mapping (UACM) with a plane wave beam. PACM can give detailed information with high sensitivity and spatial–temporal resolution, but it is time consuming and strict on the medium with repeatable cavitation distribution. UACM with a plane wave beam has a much higher frame rate than that of conventional B-mode ultrasound imaging, and thus, it can map the transient behaviors of bubbles over the entire region at once. In addition, three-dimensional (3D) plane-by-plane cavitation mapping can be achieved by sequentially measuring a series of such planes where the linear array at each unit is positioned perpendicular to the axis of the cavitation source.

Because UACM uses a plane wave beam rather than a focused pulse, the signal-to-noise ratio (SNR) and lateral resolution should be improved. One way to do this is by using minimum variance (MV) beamforming and coherence factor (CF) weighting in combination with UACM. This MVCF-based UACM can image cavitation bubbles with a relatively high SNR and good spatial–temporal resolution. However, because the primary cavitation source signal as well as the interrogating pulse may interfere with acoustic emissions from bubbles, ACM is presently performed when ultrasound exposure is off. Unlike ACM though, cavitation maps obtained by PCM are based on the emission signals from bubbles when ultrasound irradiation is on, potentially allowing for real-time spatial mapping of cavitation activity.

In this chapter, we introduce methods of cavitation detection and mapping and we describe these techniques when they are applied in water; cavitation imaging in tissues is described in Chap. 7.

2.2 Cavitation Mapping by High-Speed Photography

High-speed photography refers to technology specifically for recording very fast phenomena. In 1948, the Society of Motion Picture and Television Engineers (SMPTE) defined high-speed photography as any set of photographs captured by a camera with 128 frames per second (fps) or greater. At present, ultrahigh-speed photography can achieve as high as 200 million fps in an exposure time of 5 ns. In common applications, high-speed photography may refer to either one or both types of meanings: High-speed photography can refer to a single frame that is taken to freeze motion, especially to reduce motion blur, or it can refer to a series of photographs that are taken at a high sampling frequency. By the first meaning, high-speed photography requires a sensor with good sensitivity and either a very good shuttering system or a very fast strobe light. In the second case, it requires some means of capturing successive frames, either with a mechanical device or by loading data from electronic sensors very quickly.

The first practical application of high-speed photography was Eadweard Muybridge's 1878 investigation into whether horses' feet were actually all off the ground at once during a gallop. Later, in 1886, the first photograph of a supersonic flying bullet was taken in Rijeka by the Austrian physicist Peter Salcher, which afterward was used by Ernst Mach in his studies of supersonic motion. Many decades later, high-speed photography was employed to capture instantaneous phenomenon in many research fields, and it is now also used to view ultrasound- and laser-induced cavitation bubbles. To better understand the effects cavitation bubbles produce, considerable effort has been applied to study the behavior of cavitation bubbles, such as their oscillations, translator motion, collapse, disintegration, and coalescence, under various conditions. For a long time, high-speed photography has been the only method available to perform these investigations, and in the following sections, we discuss how it has been applied.

2.2.1 Single-Bubble Cavitation

2.2.1.1 Free Field

In 1989, Leighton et al. (1989) presented two image series showing the unstable growth and collapse of bubbles much smaller than resonance size, where images were captured by a Hadland Hyspeed camera. The camera had a maximum frame rate of about 8000 fps for full-frame photography, taking about 1 s of film in real time. With these images, they verified the predictions of the earlier numerical solutions. Bubbles just smaller than resonance size (which represents a radius 0.3 mm in a 10-kHz sound field) were seen to undergo stable cavitation; much smaller bubbles grow and collapse unstably.

Lauterborn and Ohl (1997) employed an image converter camera to take a photographic series showing the collapse of a laser-generated spherical bubble in water. Its frame rate reached 20.8 million fps. With this high frame rate, the shock wave radiated upon bubble collapse was easily captured. And in 2001, a high-speed camera (Imacon 700, Hadland Photonics) with 22,700 fps was employed by the same group to take 18 consecutive frames, as shown in Fig. 2.1, in which bubble expansion, contraction, and collapse were presented (Akhatov et al. 2001).

2.2.1.2 Fluid–Rigid Boundary

When a bubble is collapsing in a non-spherically symmetric environment, the situation changes considerably. A flat surface nearby causes the bubble to involute from the distal end and to develop a high-speed liquid jet toward this solid surface. However, the distance between the bubble's proximal end and the solid surface may result in different jet shapes.

In the 1982 Ultrasonics Symposium, famous high-speed photograph of a single bubble was presented (Fig. 2.2) by Prof. L.A. Crum. This image shows the liquid jet produced during collapse of a cavitation bubble with a diameter of 1 mm on a solid surface. The width of the bubble was about 1 mm (Crum 1982).

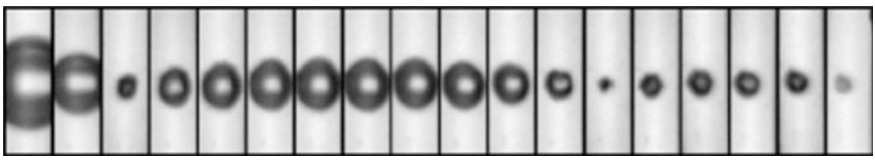

Fig. 2.1 High-speed series of bubble dynamics shortly before and after the first collapse. The interframe time and exposure time were 4.4 and 1 μs, respectively. Reproduced with permission from Akhatov et al. © American Institute of Physics

Fig. 2.2 Cavitation jet developed in a single bubble. Reproduced with permission from Crum et al. © IEEE

As the distance between a bubble and solid surface increases, the length of the liquid jet increases as well. W. Lauterborn's group presented a series of bubble collapsing photographs taken at 75,000 fps with a rotating mirror camera (Lauterborn and Ohl 1997). The jet could be visualized when the bubble was in the first rebound phase. As shown in Fig. 2.3, the dark line inside the bright central spot of the bubble is the same as that shown in Fig. 2.2. However, the difference is that the funnel-shaped downward protrusion shown in Fig. 2.3 is the elongated bubble wall containing the jet, which is driving the elongation.

In this study, each growth and collapse was suggested to take about 50 μs for the smallest bubbles (radius <0.5 μm) and 3–4× longer for larger bubbles (radius 0.15 ± 0.05 mm). Furthermore, the group predicted that the bubble sizes reached during stable cavitation were similar to earlier predictions. However, an exact correlation was not possible since the initial bubble radii could only be estimated from the high-speed photographs, and stable cavitation is highly nonlinear and very sensitive to the initial bubble size.

2.2.1.3 Free Fluid Surface

Another case that has received extensive attention is pulsating bubbles below a free surface (Cole 1965; Holt 1977). Robinson and Blake et al. (2001) presented the experimental effects of nonlinear interactions on the motion of a single bubble and a free surface using high-speed photography (Fig. 2.4).

A striking free-surface–bubble interaction is shown in Fig. 2.5 for a bubble that was generated at just more than one-half of its maximum radius from the free surface (Robinson et al. 2001). The bubbles were generated by an electrical discharge, and the images clearly show the development of both the free-surface spike and the liquid jet.

To observe single-bubble cavitation dynamics, high-speed photography is always used in conjunction with a microscope, such as an inverted microscope or a long-distance microscope, but the specific use depends highly on the cavitation situation.

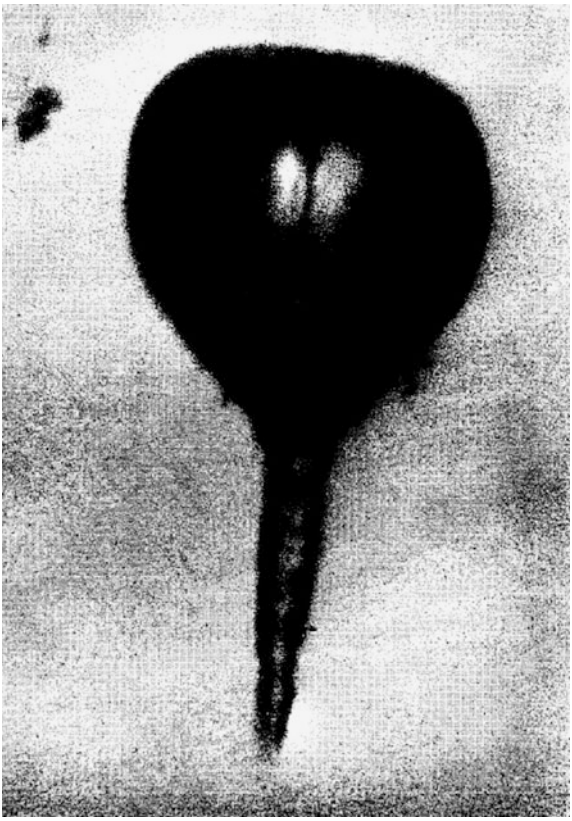

Fig. 2.3 Enlargement of a bubble with a jet and its protrusion pointing to the solid boundary. Reproduced with permission from Lauterborn et al. © Elsevier

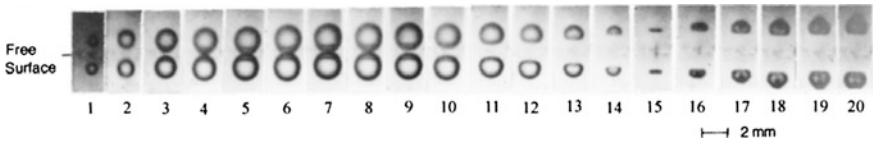

Fig. 2.4 High-speed photographs of a single bubble generated at a dimensionless distance beneath a free surface. Frame interval, 10 μs; exposure time, 2 μs. Reproduced with permission from Robinson et al. © American Institute of Physics

2.2.2 Multiple-Bubble Cavitation

Turning now to studying the inception of cavitation and the large-scale distribution of cavitation bubbles, high-speed photography has also been used to visualize multiple-bubble cavitation, especially in focused ultrasound fields. Focused ultrasound is characterized by its ability to noninvasively penetrate deep into the human

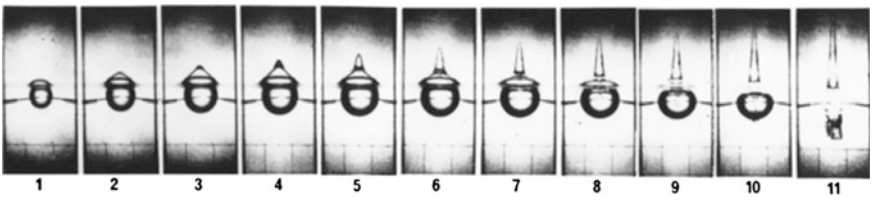

Fig. 2.5 High-speed photographs of a single bubble generated by an underwater electrical discharge at a dimensionless distance beneath a free surface. Reproduced with permission from Robinson et al. © American Institute of Physics

body and precisely deliver energy to a specific site (Vaezy et al. 2001a). Because of its high energy concentration, focused ultrasound represents a cavity source for multiple bubbles. In various applications of ultrasound in water, cavitation bubble clouds organize into different structures, and high-speed photography has been very useful for investigating the dynamics of these bubbles.

Luther et al. (2001) observed branchlike patterns of cavitation bubbles induced by an acoustic resonator in the 20 kHz frequency range, and they used a 2250-fps high-speed camera to observe the bubbles. In another study, Moussatov et al. (2003) discovered a conelike bubble structure in the vicinity of a transducer radiating surface with a frequency of 20.7 kHz, and they used high-speed images to reveal the process through which this structure was built.

Also studying multiple-bubble cavitation, Chen et al. (2006a, b) documented the temporal evolution of a cavitation bubble cloud in a 1.2-MHz focused ultrasound field and investigated the emergence of the cloud in the focal region, as shown in Figs. 2.6 and 2.7, respectively.

After analyzing these images, the authors gave two possibilities for why cavitation initiated in the prefocal region. First, in the prefocal region, some secondary pressure peaks exist, especially in the area near the focal region. Meanwhile, cavitation bubbles in the focal region may reflect ultrasound energy into the prefocal region. For example, cavitation bubbles generated at the transducer surface are driven by radiation forces to the focal region. When they move upward, the high pressure causes them to expand and fragment to small bubbles which, in turn, grow larger, resulting in the augmentation of the bubble clouds. At the same time, they are attracted to each other and form bubble clusters by the secondary Bjerknes forces. Gradually, the bubble cloud accumulates to a visible size in the prefocal region.

Chen et al. (2006a) did additional studies focused on the inception of cavitation bubble clouds induced by high-intensity focused ultrasound (HIFU). As shown in Fig. 2.8, they found that cavitation bubbles may be visible in the prefocal regions because the cavitation bubbles near the focus might shield the upper bubbles (post-focal regions) from oscillating to detectable size.

The inertial 145 μs of bubble inception in HIFU focus was also investigated by the authors (Chen et al. 2006a). They found that the whole bubble cloud was formed at 85 μs, and it then remained stable for at least 60 μs. The radiation forces

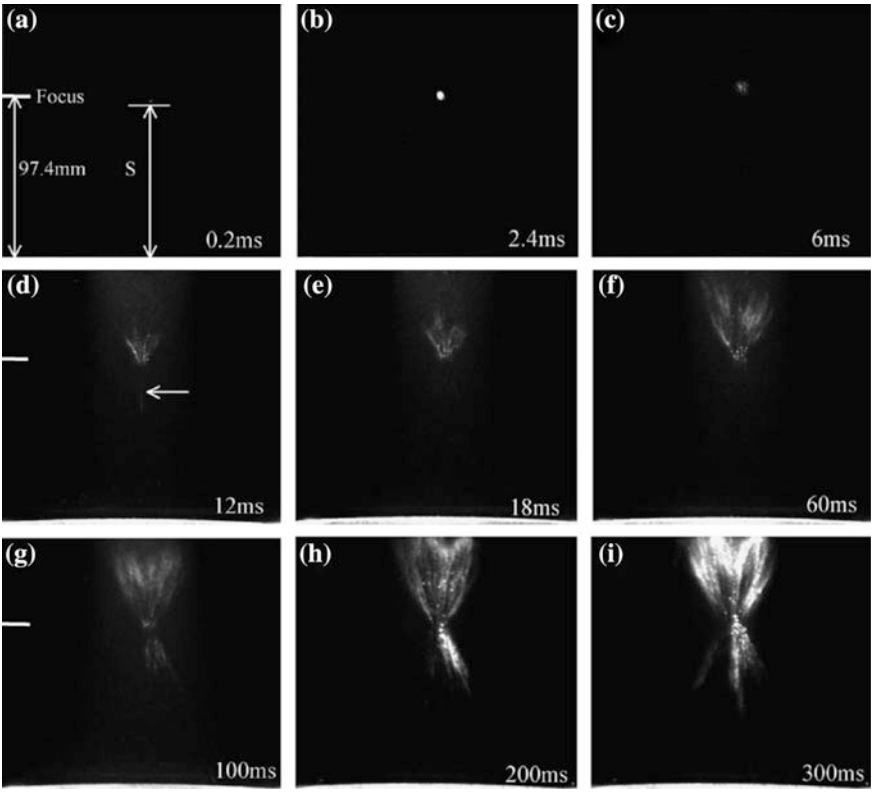

Fig. 2.6 High-speed images of the formation of a cavitation bubble cloud captured at different delay times (indicated in the *right* corner of each image). Reproduced with permission from Chen et al. © Elsevier

produced only a slight upward movement, which is visible on the streak image shown in Fig. 2.9. The axial maximum displacement was about 0.9 mm achieved by the bubble nearest to the focus (as pointed out by the arrowhead). Therefore, the bubbles seemed to be in a stable dynamic equilibrium.

Another application that employs multiple-bubble cavitation produced by focused ultrasound that has been investigated in recent years is pulsed HIFU-induced tissue erosion. The temporal evolution and spatial distribution of cavitation bubble clouds in the focal region have been studied by several groups. In 2008, Xu et al. (2008) studied the evolution of bubble clouds generated by a histotripsy pulse (10 and 14 acoustic cycles) with the help of an intensified charge-coupled device (ICCD). In the next year, Chen et al. (2009) employed ultrahigh-speed photography to capture the inception of a cavitation bubble cloud in the focal region of a tissue's surface, and they obtained two structures of bubble clouds, and the interchanging between these two bubble cloud structures are shown in Fig. 2.10.

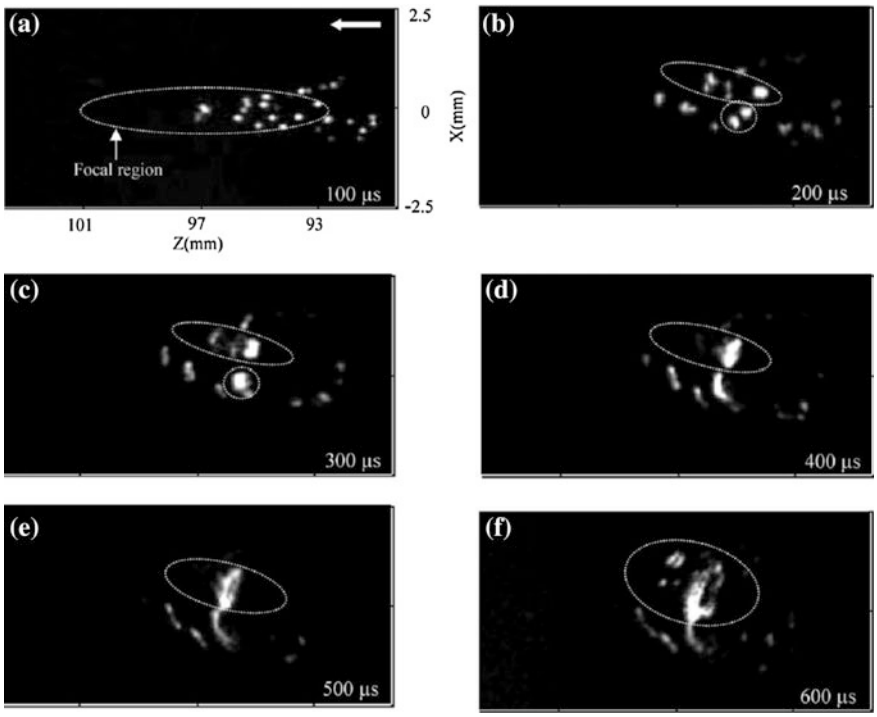

Fig. 2.7 High-speed images (exposure time, 10 µs; captured in 100-µs steps) showing the generation, mergence, and collapse of cavitation bubbles. Reproduced with permission from Chen et al. © Elsevier

2.2.3 Cavitation in Microvessel

Turning to the biomedical field, cavitation in microvessels must be understood well because ultrasonic contrast agents are usually delivered in microvessels. To study this, Chomas et al. (2001) investigated the behavior of lipid microbubbles (MP1950) in cavities. Figure 2.11 is a set of seven frames and a streak image of a microbubble undergoing Rayleigh–Taylor instability and its resultant fragmentation. Figure 2.11a shows the microbubble before insonation, with a resting diameter of 3 µm. The ultrasonic pulse is a two-cycle sinusoid, with a peak negative transmission pressure of 1.2 MPa. The microbubble is shown at the peak expansion of the first cycle in Fig. 2.11b, with a diameter of 10 µm. Figure 2.11c, d shows the microbubble during compression after the first expansion, while it is still intact. Due to the high velocity experienced by the wall during the end of compression, Fig. 2.11d appears blurred in both the frame and the streak. The microbubble fragments near the peak compression, and the result of this process is shown as a group of six fragments in Fig. 2.11e, f. Figure 2.11g shows the microbubble after the end of insonation, after three of the fragments observed in Fig. 2.11f dissolved.

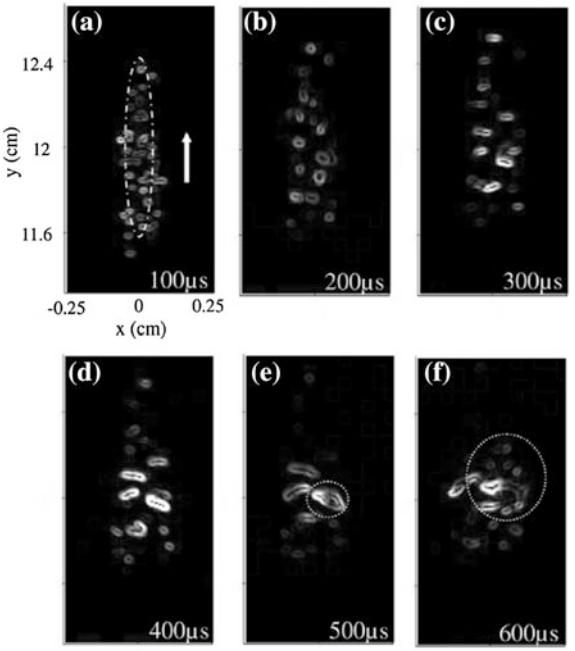

Fig. 2.8 High-speed images showing the dynamics of cavitation bubbles within the initial 600 μs. Reproduced with permission from Chen et al. © Elsevier

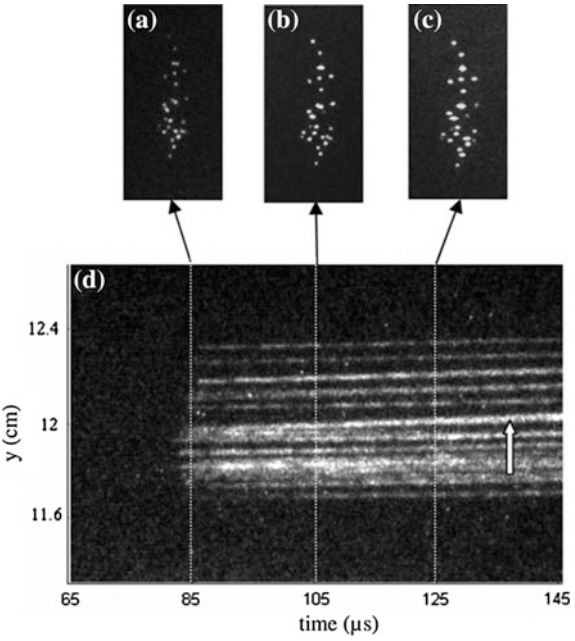

Fig. 2.9 Still images photographed at different times after the onset of ultrasound transmission: **a** 85 μs, **b** 105 μs and **c** 125 μs. Reproduced with permission from Chen et al. © Elsevier

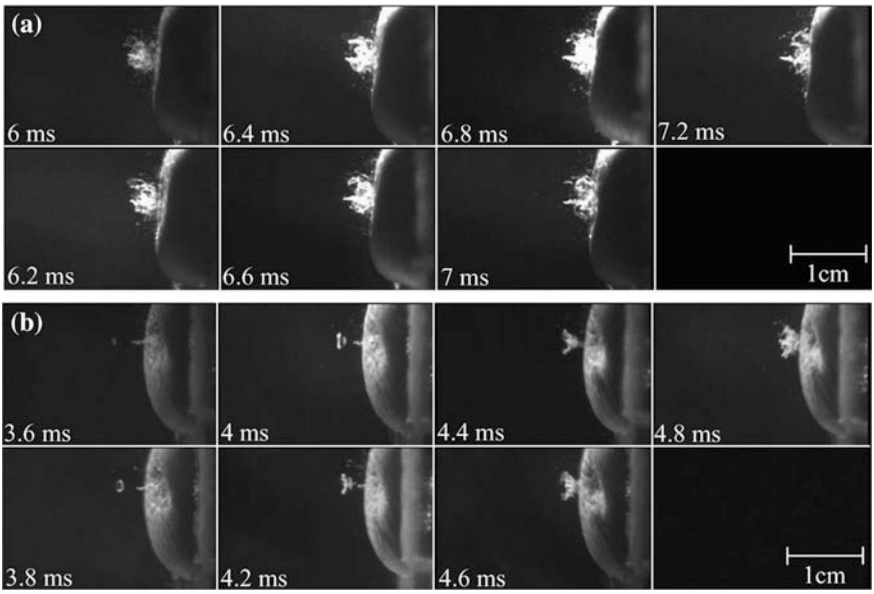

Fig. 2.10 Bubble cloud structures on tissue surfaces. **a** A crown-shaped bubble cloud developed into a cone-shaped bubble cloud. **b** A cone-shaped bubble cloud changed to a crown-shaped bubble cloud. Reproduced with permission from Chen et al. © Elsevier

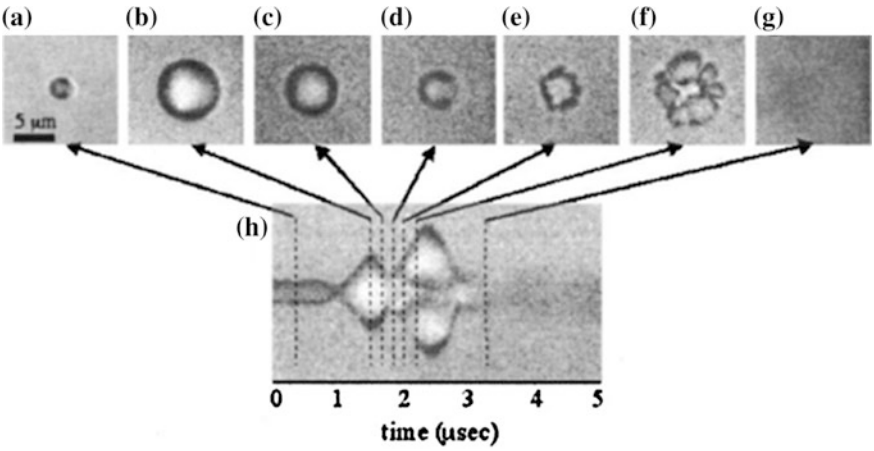

Fig. 2.11 Optical frame images and a streak image corresponding to the oscillation and fragmentation of a contrast agent microbubble, where fragmentation occurred during compression. The microbubble has a resting diameter of 3 μm shown in (**a**). The streak image in (**h**) shows the diameter of the microbubble as a function of time, and the lines indicate the times at which the two-dimensional (2D) frame images in (**a**–**g**) were acquired relative to the streak image. Reproduced with permission from Chomas et al. © Society of Photo-Optical Instrumentation Engineers

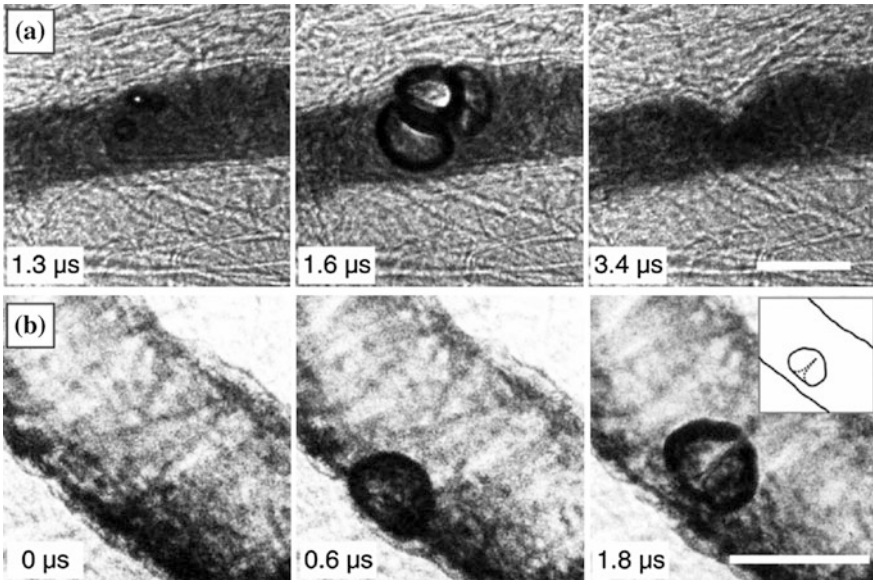

Fig. 2.12 Characteristics of observed bubble–vessel interactions. Reproduced with permission from Chen et al. © American Physical Society

Chen et al. (2011) also made two primary observations about how acoustically excited bubbles interact with microvessels in ex vivo tissue. They found that vessel deformation favored invagination over distention and that the liquid jets formed during collapse were directed away from the nearest vessel wall. As shown in Fig. 2.12, the qualitative characteristics of such bubble–boundary interactions are expected to be sensitive to the mechanical properties of the boundary material. Because the mechanical properties of tissue remain incompletely understood (especially for strains and strain rates relevant to medical ultrasound), these observations identify how bubbles are likely to interact with real vessels.

2.3 Cavitation Mapping by Sonoluminescence and Sonochemiluminescence

As a powerful tool to visualize the spatial distribution and dynamics of cavitation bubbles (Chen et al. 2006b), high-speed photography can capture all cavitation bubbles in a cloud. However, optical devices that detect bubbles' SL and SCL emissions can provide more information about the spatial distribution of chemically active cavitation bubbles (Cao et al. 2012; Suslick 1990).

SL, a phenomenon generally attributed to the high temperatures generated during the collapse of cavitation bubbles, can be observed as short light pulses

occurring once every acoustic period (Gaitan et al. 1992). When observed through a microscope, these emissions can be seen to originate at the geometric center of the bubble, and they likely occur simultaneously with bubble collapse. SL in single bubbles (single-bubble sonoluminescence SBSL) has also been investigated using acoustically trapped and periodically driven gas bubbles (Gaitan et al. 1992). In these studies, when the bubble collapses strongly, the energy released at collapse leads to light emission. However, the light intensity is quite weak and thus difficult to detect. As a result, various photosensitizers must be used to enhance the light emission without changing the cavitation mechanisms.

2.3.1 Mechanisms of SL and SCL

Adiabatic collapse of an active cavitation bubble generates extremely high local temperatures and pressures. The extreme conditions within active cavitation bubbles can lead to SL light emission, as discussed previously. However, when luminol is added to an alkaline solution, it can significantly enhance the light intensity. This phenomenon is referred to as SCL, and it is identical to chemiluminescence that occurs in bulk liquid regions when induced by the chemical reaction of luminol molecules with $HO^{\cdot}$ radicals. When ultrasonic irradiation is applied to an alkaline luminol solution, the sonochemical effects of molecular activation and dissociation take place within the active cavitation bubble or at the solution layer near the bubble.

2.3.1.1 Sonochemical Reactions in Air-Saturated Water (McMurray and Wilson 1999)

In air-saturated water, the hemolytic cleavage of H_2O and dissolved O_2 occurs:

$$H_2O \rightarrow H^{\cdot} + HO^{\cdot}$$
$$O_2 \rightarrow O + O$$

The cleavage products may then recombine or react further as below:

$$HO^{\cdot} + HO^{\cdot} \rightarrow H_2O_2$$
$$O + H_2O \rightarrow HO^{\cdot} + HO^{\cdot}$$
$$H^{\cdot} + O_2 \rightarrow HO_2^{\cdot}$$
$$HO_2^{\cdot} + HO_2^{\cdot} \rightarrow H_2O_2 + O_2$$

Both $HO_2^{\cdot}$ and H_2O_2 are weak acids, so in conditions of neutral and higher pH values, the dissociation processes are as follows:

$$HO_2^{\cdot} \rightleftharpoons H^+ + O_2^{\cdot -}$$
$$H_2O_2 \rightleftharpoons H^+ + HO_2^-$$

The hydroxyl radicals ($HO^{\cdot}$) have the potential to oxidize both HO_2^- and H_2O_2. Thus, in the presence of significant concentrations of H_2O_2 in a sonicated solution, the following two reactions become dominant:

$$HO_2^{\cdot} + H_2O_2 \rightarrow O_2^{\cdot -} + H_3O^+$$
$$HO^{\cdot} + HO_2^- \rightarrow O_2^{\cdot -} + H_2O$$

2.3.1.2 Luminol SCL Mechanism (McMurray and Wilson 1999)

Luminol, with the structural formula as shown in Fig. 2.13, is a weak dibasic acid with first and second pKa values of 6.3 and ~13, respectively. In an alkaline solution, the luminol molecule will dissociate into a luminol monoanion (I) through the following two processes.

Then, the luminol monoanion can be oxidized by hydroxyl radicals ($HO^{\cdot}$) to produce the diazaquinone radical anion (II), as shown in Fig. 2.14 step (i). In step (ii), compound II reacts with the $O_2^{\cdot -}$ radical anion to form the hydroperoxide addition product (III), which is a weak acid with a pKa of 10.4. The monoanion form of compound III can decompose through step (iii) to give the exited state of the aminophthalate monoanion (IV), while the neutral form of III decomposes via a dark reaction (iv) to generate the starting material (I) and O_2. The excited aminophthalate monoanion IV molecule can then relax into the ground state by emitting light at 430 nm.

Even though the mechanism of SL still remains unclear, many investigations during the last few decades have tried to uncover it. Since 1934, when Frenzel and Schultes (1934) first documented the phenomenon of multi-bubble

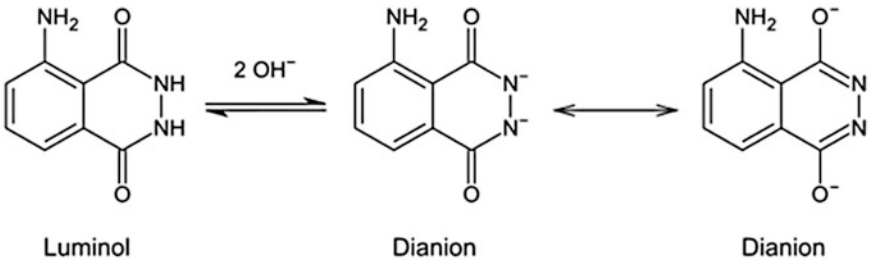

Fig. 2.13 Structural formula and dissociation of luminol

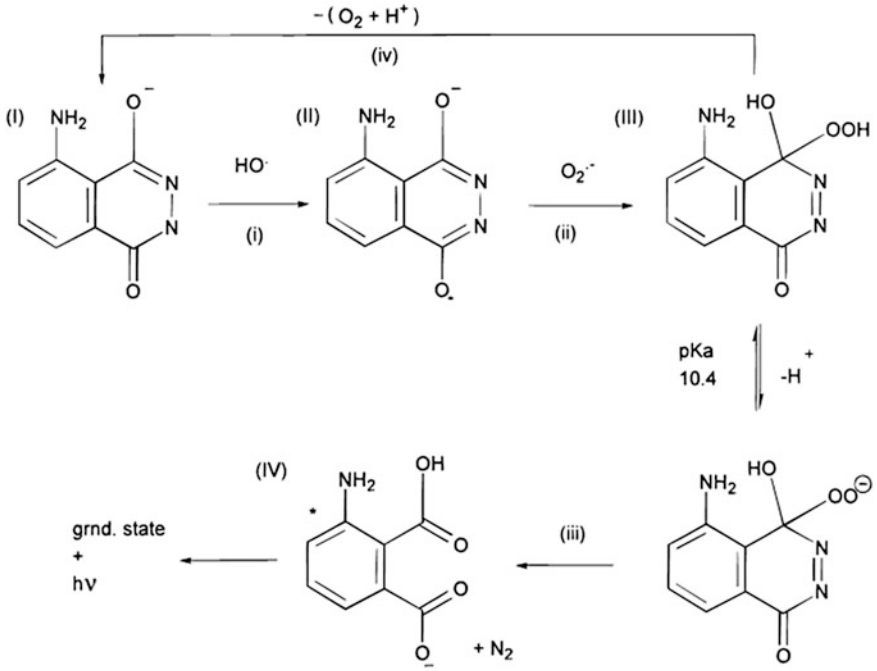

Fig. 2.14 Schematic showing the principal mechanism of sonochemiluminescence

sonoluminescence (MBSL) in ultrasonic fields, various hypotheses have been put forward to explain the origin of the light emission. For example, Chambers (1936) put forward a triboluminescence theory as early as 1936. However, with the advent of SBSL in 1989, studies on the mechanisms of SL have improved, causing many of the early theories to fall out of favor and even become abandoned.

In the next four sections, we describe the most popular and most recognized theories for the mechanisms of SL.

2.3.1.3 Hot Spot Theory

In "hot spot" theories, the energy for light emission is thought to originate from the thermal energy released in the adiabatic process of bubble collapse. These theories rely on the fact that light emission preponderantly depends on the maximum temperatures reached within the cavitation bubbles, because the recombination of dissociated molecules that can accompany light emission and the characteristic molecular radiation of light emission can occur at extremely high temperatures (Brenner et al. 2002). Thus, these hot spot theories can be supported by the findings presented by Noltingk and Neppiras (1950), and Neppiras and Noltingk (1951) who used the Rayleigh–Plesset equation of bubble dynamics to deduce that adiabatic

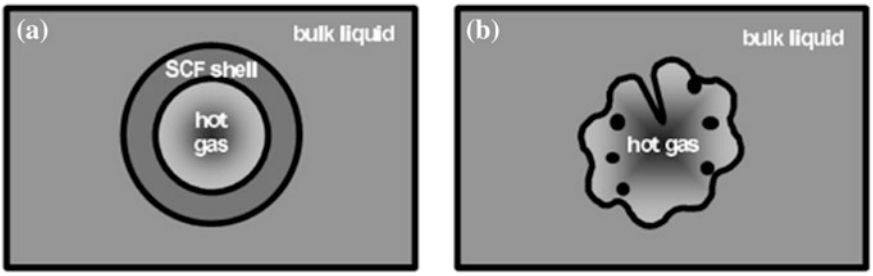

Fig. 2.15 The two-site models of sonochemical reactions. **a** The thermal diffusion shell model. **b** The surface-wave distortion and jet model. Reproduced with permission from Suslick et al. © Wiley Online Library

compression of a bubble's contents can produce temperatures of 5000 to 10,000 K. More recently in the past few decades, Kenneth Suslick and colleagues have amassed impressive evidence in favor of thermal molecular emission luminescence (Brenner et al. 2002). For example, Suslick (1986, 1990) deduced the thermal origin of MBSL from the SL spectrum, in which molecular bands can be clearly identified while lines associated with discharges do not exist. He has also proposed that there are in fact two sonochemical reaction sites shown in Fig. 2.15. The first (the dominant site) is the bubble's interior gas phase, whereby a hot liquid shell is formed around the surface of the gas bubble. The second reaction site is initially liquid and corresponds either to the heating of a shell of liquid around the collapsing bubble or to the injection of liquid droplets into the hot spot by surface-wave distortions or jets of the collapsing bubble (Suslick et al. 1999).

While hot spot theories are supported by compelling evidence, there is no clear definition of a "hot spot" in physics, so the origin of the light emission in SL cannot be completely explained by such theories.

2.3.1.4 Blackbody Theory

Another theory for the mechanism of SL was introduced by Jarman (2005), who has described that luminescence occurs from microshocks that are thermal in origin and have a spectral distribution that closely resembles that of a blackbody. In addition, Vazquez et al. (2001) measured the spectral irradiance, Mie scattering, and flash width of SL occurring from bubbles of hydrogen gas and noble gasses, and they suggested that the light emission was actually the radiation from a blackbody with temperatures ranging from 6000 K (H_2) to 20,000 K (He). For a mixture of hydrogen and water, as shown in Fig. 2.16, the radius of a bubble surface for light emission is about 0.2 μm, and the SL spectrum can match that of a blackbody at 6230 K.

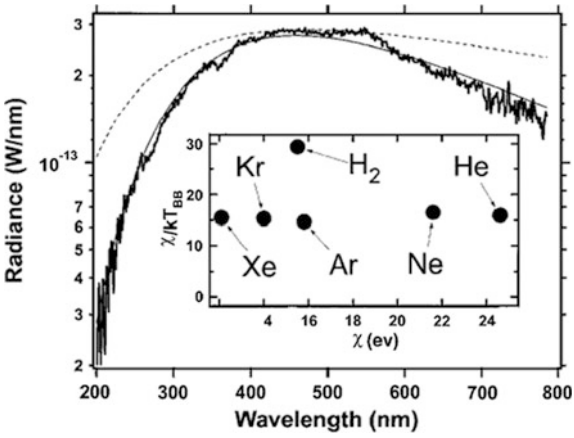

Fig. 2.16 Spectrum (resolution, 24 nm FWHM) of 33-kHz SL from a bubble formed in water (23 °C) into which H_2 was dissolved at a partial pressure of 5 Torr. The solid curve is fit to a blackbody at 6230 K. The dashed curve represents a bremsstrahlung fit with a temperature of 15,000 K. The inset shows a plot of χ/TBB as a function of χ, the ionization potential of the gas used to produce the SL. Reproduced with permission from Vazquez et al. © Optical Society of America

2.3.1.5 Bremsstrahlung

Bremsstrahlung is another theory that can be used to explain the mechanism of SL. Bremsstrahlung is the radiation produced when an electrically charged particle, especially an electron, is slowed down by the electric field of an atomic nucleus or an atomic ion. In accordance with Young's book (2004), there are three kinds of bremsstrahlung. (1) Electron ion bremsstrahlung is the light emission from an electron slowed down in the Coulomb field of a positive ion. (2) Electron atom bremsstrahlung is the bremsstrahlung that occurs when an electron passes through the field of a neutral atom. The field of a neutral atom decreases rapidly with distance, and therefore, the electron must pass very close to the atom to ensure the emission of light. (3) Finally, polarization bremsstrahlung is similar to the electron atom bremsstrahlung, but the main difference is that the neutral atom is polarized in the Coulomb field.

In 1998, Frommhold (1998) suggested that electron-neutral atom bremsstrahlung may be a principal mechanism for the SL from rare gas bubbles in a weakly ionized environment. Supporting this, Yasui (1999) later showed that SL mainly occurs via radiative recombination of electrons and ions, and electron atom bremsstrahlung.

In a different study that investigated an argon gas bubble, Xu et al. (1998, 1999, 2000) found that atoms inside a very thin layer of plasma around the bubble's origin were strongly ionized, and the SL occurred nearly simultaneously. They concluded that multiple ionization and recombination played a dramatically important role in SL.

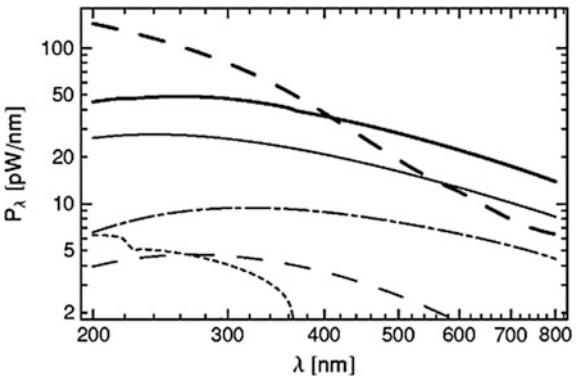

Fig. 2.17 An SBSL spectrum and its composition for argon bubbles in water at freezing temperatures. Shown in the total spectrum (*thick solid line*), electron-neutral argon bremsstrahlung (*thin solid line*), O^-radiation (*dotted line*), H^- radiation (*dashed line*), and e-Ar^+ bremsstrahlung (*dash dotted line*). The measured spectrum is indicated by the *thick dashed line*. Reproduced with permission from Hammer et al. © American Physical Society

Hammer and Frommhold (2002) have made steady contributions, and they have conclude that in conventional single-bubble sonoluminescence, electron ion bremsstrahlung amounts to but a small percentage of the overall emission and that electron-neutral bremsstrahlung is likely to be the principal radiative mechanism. Figure 2.17 shows a spectrum computed from Hammer and Frommold's model for argon bubbles in freezing water. The predominance of electron-neutral bremsstrahlung is shown.

2.3.1.6 Shock Wave Theory

Finally, shock wave theory has also been used to explain SL. This theory assumes that extreme temperatures can be attained by spherical microshocks propagating within the imploding bubble as they converge toward the center of the bubble (Taylor and Jarman 1970), and the extreme temperatures can accelerate the dissociation process of molecules, generating high-speed free electrons and ions. Then, these high-speed free electrons and ions can collide, producing the light emission seen in SL.

To deduce that a shock forms during bubble collapse, Greenspan and Nadim (1993) used the governing equations of gas dynamics inside a bubble. They also found that this converging spherical shock grows in strength as it propagates toward the center.

Later, Moss et al. (1994) performed numerical hydrodynamic simulations of the growth and collapse of a 10-μm air bubble in water using a plasma model composed of a thermal conductive component and a partially ionized component. They calculated the light pulse duration time and the spectrum character, and they

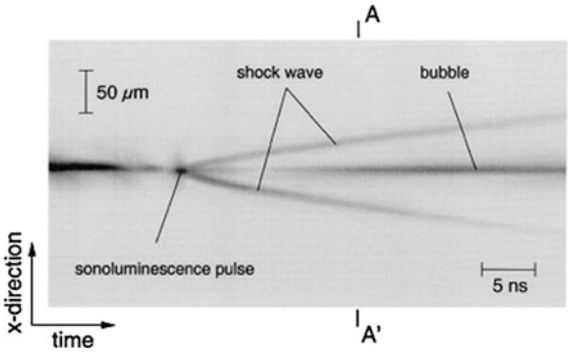

Fig. 2.18 Streak image of the SBSL bubble collapse. The time and space axis are marked by arrows, and the dark parts of the image correspond to high light intensity. Reproduced with permission from Pecha et al. © American Physical Society

concluded that a nuclear fusion reaction temperature can be achieved by the addition of the converging shock wave and an extra pressure pulse.

Further supporting the shock wave theory, Pecha and Gompf (2000) used a streak camera with high spatial and temporal resolution to image the dynamics of the violent collapse in SBSL. Figure 2.18 shows their recorded streak image of the end phase of the bubble collapse, in which the shock wave was formed.

Putterman and Weninger (2000) summarized that light comes out only while the plasma exists. The light emission is thermal bremsstrahlung from the accelerating free electrons. These electrons will accelerate and radiate light as they collide with the ions.

2.3.2 Free Field

SL responses have also been studied in free fields. Cao et al. (2012) reported results of SL by an ICCD camera with a 30-s exposure time in a 1.2-MHz focused ultrasound field in degassed water. They varied the electrical power level from 30 W to 50 W to 70 W as shown in Fig. 2.19, from which we can see that the SL emissions were mainly located in the post-focal region, where the density of chemically active cavitation bubbles was high.

Because the active SL bubbles grow during the expansion phase, the temperature required for SL emissions is higher, while the temperature for SCL emissions remains relatively low. Therefore, the sonochemically active region and time period are larger in comparison with SL, and the intensity of SCL is 10–100× higher than that produced by SL (Hatanaka et al. 2000).

Thus, Cao et al. (2012) also acquired SCL images under the same experimental conditions as the SL experiments shown in Fig. 2.19, as these SCL results are shown in Fig. 2.20. Compared with Fig. 2.19, the SCL region is more extensive and has higher light intensity. Also, the SCL images showed branchlike shapes

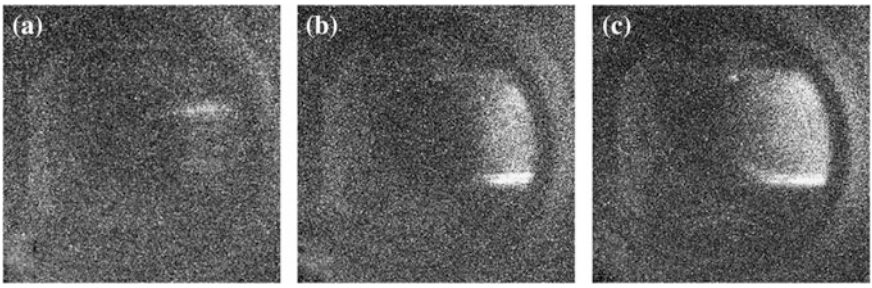

Fig. 2.19 SL images acquired by an ICCD camera at the same exposure time (30 s) but with different electrical powers: **a** 30 W, **b** 50 W, and **c** 70 W. The ultrasound wave was transmitted from the *left* to the *right* side. Reproduced with permission from Cao et al. © Elsevier

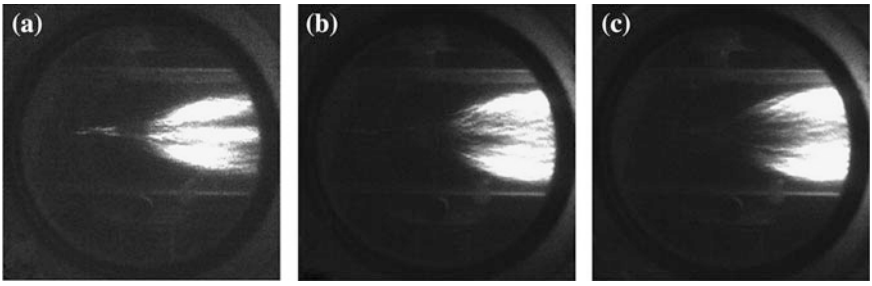

Fig. 2.20 SCL images at the same exposure time (30 s) with different electrical powers: **a** 30, **b** 50 W, and **c** 70 W. Reproduced with permission from Cao et al. © Elsevier

corresponding to the distribution of cavitation bubbles obtained by the high-speed camera (H. Chen et al. 2006b).

In a different SCL experiment, Hallez et al. (2010) presented SCL images from a digital camera with a exposure time 10 s, in which cavitation bubbles were localized in a 3-MHz focused ultrasound field. As can be noted in Fig. 2.21a, there were no obvious SCL emissions in the vicinity of the transducer and downstream of the acoustic propagation axis, and this corresponds to the fact that no active cavitation bubbles existed in those regions, shown in the tomographic image in Fig. 2.21b. Using an optic fiber to count the photons emitted, Hallez et al. quantitatively verified that the intensity of SCL emissions increased with the irradiation power, as shown in Fig. 2.22. And also, an important concept "oversaturation" was raised by L. Hallez.

2.3.3 Tissue–Fluid Interface

Cavitation is considered to be the most predominant mechanism for tissue erosion during HIFU treatments (Cao et al. 2012). Therefore, studies aimed at investigating

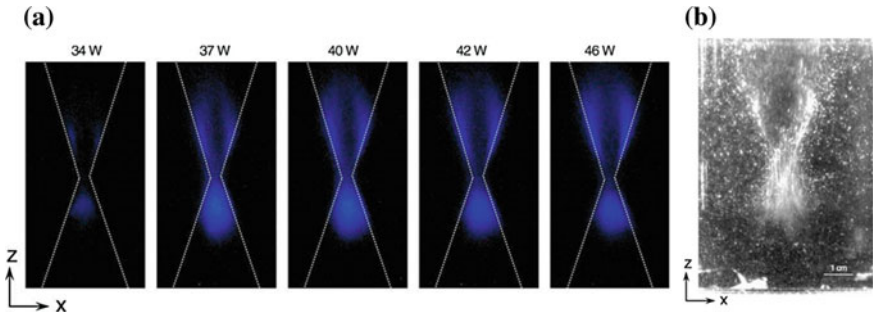

Fig. 2.21 **a** SCL for different powers. **b** Dynamics of cavitation bubbles for high-power irradiation (40 W). The transducer is located at the bottom of the picture. Reproduced with permission from Hallez et al. © Elsevier

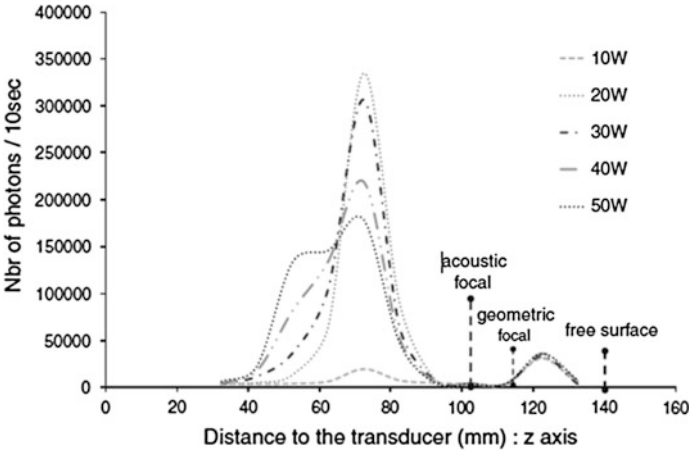

Fig. 2.22 Photon counting with an optic fiber. Reproduced with permission from Hallez et al. © Elsevier

the distribution of cavitation bubbles close to a tissue boundary are important. However, traditional acoustic detection methods and high-speed photography cannot necessarily capture active cavitation. To circumvent this issue, Cao et al. (2013) performed cavitation mapping close to a tissue–fluid interface by using SCL. Figure 2.23a shows a photograph of the tissue–fluid interface, while Fig. 2.23b–f shows the SCL images captured by an electron multiplying charge-coupled device (EMCCD) camera with a 0.5-s exposure time under various HIFU pulse lengths with a constant duty cycle of 1:10.

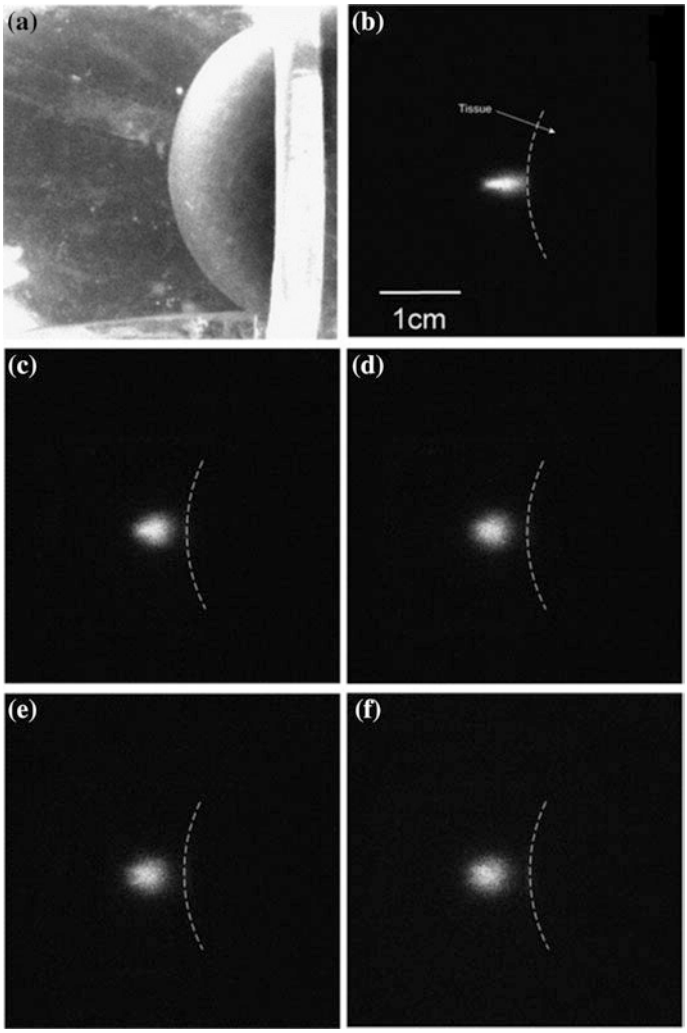

Fig. 2.23 **a** Photograph of the tissue–fluid interface. **b–f** SCL images at a tissue–fluid interface with different pulse lengths: **b** 10 μs, **c** 20 μμs, **d** 40 μs, **e** 60 μs, and **f** 80 μs. The ultrasound wave was transmitted from the *left* to *right* side in the images. Reproduced with permission from Cao et al. © Elsevier

2.3.4 Bone–Fluid Interface

Compared with soft tissues, the acoustic properties of hard tissues—bones, for example—are quite different. Hence, investigations on the cavitation bubble distribution near fluid boundaries with bones are also needed. Zhang et al. (2013) gave an account of the spatial distributions of SCL near the front surface of a bovine

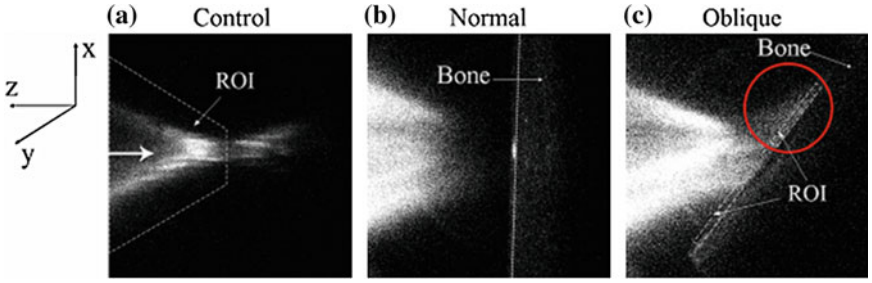

Fig. 2.24 **a** Control group: SCL emissions without the bone. **b** SCL emissions near the front surface of the bone with a normal incidence. **c** SCL emissions with an oblique incidence. Reproduced with permission from Zhang et al. © Acoustical Society of America

femur exposed to HIFU radiation with a normal and an oblique incident direction. The SCL images in Fig. 2.24 were captured by an EMCCD camera with an exposure time of 15 s. By counting the photons in the trapezoid region of interest (ROI) in the prefocal area, as shown in Fig. 2.24a, we can see that the SCL intensity in front of the bone is greater than that in the control group. This can be explained by the superposition of the reflected wave on the incident wave in the axial direction. When the incident direction was adjusted from being normal to being oblique, as seen in Fig. 2.24c, the SCL emissions became stronger and directionally extended along the straight surface of the bone (indicated with the red circle in Fig. 2.24) in the opposite direction of the HIFU field propagation.

2.3.5 Microvessel

Ohl et al. (2010) developed a novel microfluidic device (Fig. 2.25) for achieving intense acoustic cavitation, and then, they reported the SCL distribution using that setup. This device has one outlet, but two inlets that form a *T*-junction to create gas–liquid interfaces, as shown in the figure inset. A specially designed piezoelectric transducer is glued onto a microscope slide next to the microfluidic device.

The authors obtained the SCL image in the microfluidic using an EMCCD camera. As noted in Fig. 2.26a, the SCL emissions only occur within the liquid phase close to the gas–liquid interfaces, where cavitation bubbles are nucleated and driven into large oscillations. They also recorded the oscillations of cavitation bubbles close to the gas–liquid interface, as depicted in Fig. 2.26b. During the maximum expansion phase (third frame of Fig. 2.26), the bubbles are pancake shaped, whereas severe deformations occur during collapse (last frame of Fig. 2.26b).

Cavitation mapping has been also performed in microreactors, by means of SL and SCL visualization. Fernandez Rivas et al. (2012) described such a setup, which

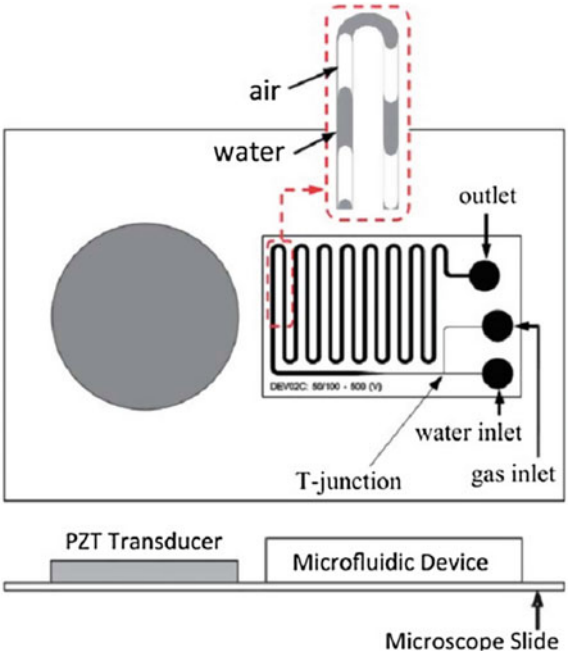

Fig. 2.25 Schematic of the microfluidic *T*-junction device and the piezoelectric transducer attached to a microscope slide. Reproduced with permission from Ohl et al. © Royal Society of Chemistry

is shown in Fig. 2.27. Here, the SL and SCL emissions are collected by the photomultiplier tube (PMT). The micromachined pits on the substrate are for nucleating and stabilizing microbubbles in a liquid.

2.3.6 Bioreactor

To study the bioeffects of ultrasound, normally experiments involve applying low-intensity ultrasound to carcinoma cells to determine how ultrasound interacts with the cells in vitro. There are several ways to position the cell holder in such experiments, but normally it is placed above the ultrasound propagation direction, as shown in Fig. 2.28. Whatever the experimental system though, it is necessary to decide the acoustic field and distribution before the cell irradiation.

The most common method to decide the acoustic field and distribution is by directly measuring them with a hydrophone. These measurements can map the acoustic pressure in the interested region. However, when using a bioreactor for cell–ultrasound interaction experiments, the cell holder is always sealed off from the surrounding degassed water, so it might be impossible to put the hydrophone in the cell holder in order to measure the acoustic pressure distribution in that area. To avoid this, published studies always give the acoustic pressure and distribution at the plane where cell holder is located (but when the cell holder is absent) instead of

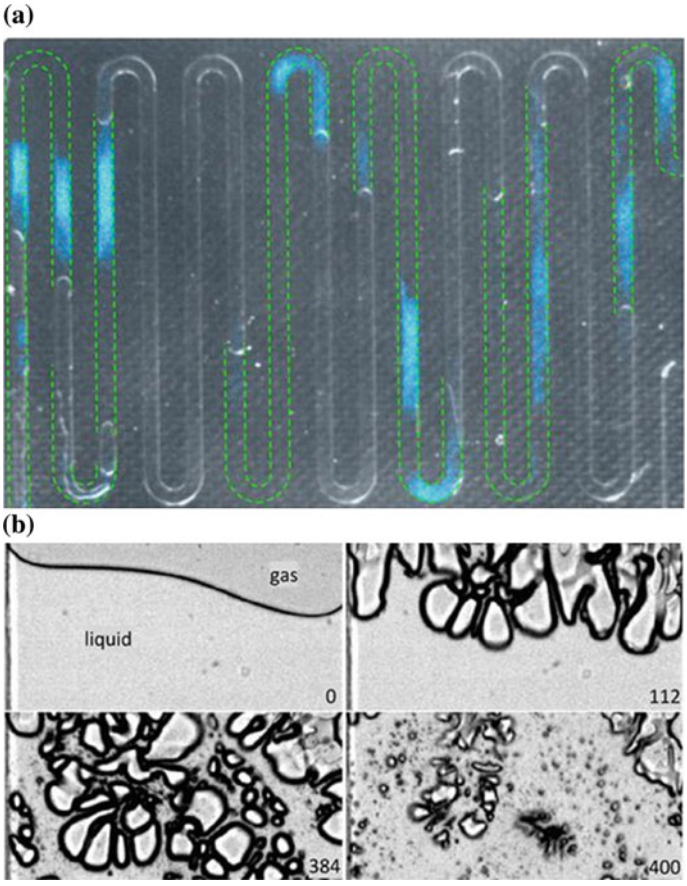

Fig. 2.26 **a** Luminol chemiluminescence from cavitation bubbles. **b** Sequence of images taken from a high-speed recording of the bubble distribution near a gas–liquid interface. Reproduced with permission from Ohl et al. © the American Association for the Advancement of Science

measuring the true acoustic pressure in the experiment. While studies do describe that the acoustic pressure and distribution might be modified by the cell holder, some suggest that these influences can be ignored, while others think the modified acoustic condition can crucially affect the results. Moreover, simulations have also been introduced to mimic the pressure distribution in the cell holder. From these studies, it is obvious that existing methods of measuring acoustic pressure and distribution do not show the true interactions between cells and ultrasound. Thus, we must develop novel methods to map the acoustic pressure in bioreactors.

Cavitation is one of the main factors resulting from low-intensity ultrasound that affects cells. Thus, cavitation mapping in the bioreactor is important for describing the true cavitation environment around cells and it can be used to further analyze the effects of cavitation on cells during ultrasound irradiation. Using SCL in a

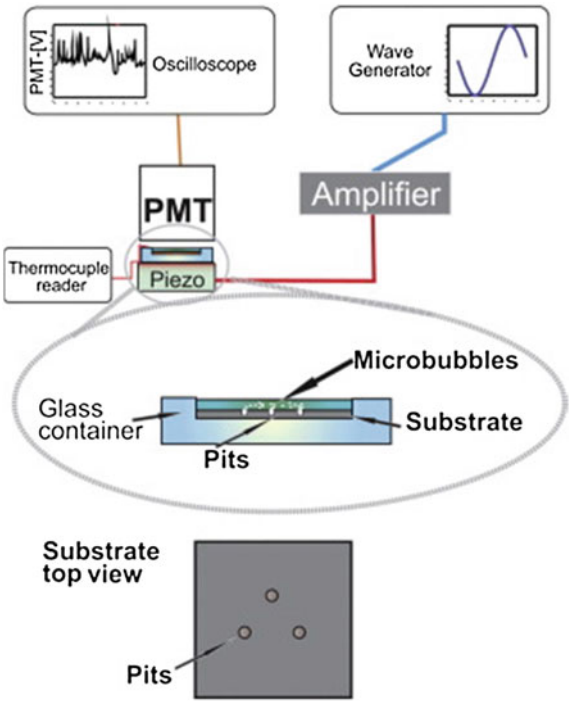

Fig. 2.27 Experimental setup (not to scale) showing the different components. The zoomed inset shows the microreactor and a *top* view of a three-pit substrate. Reproduced with permission from Rivas et al. © Elsevier

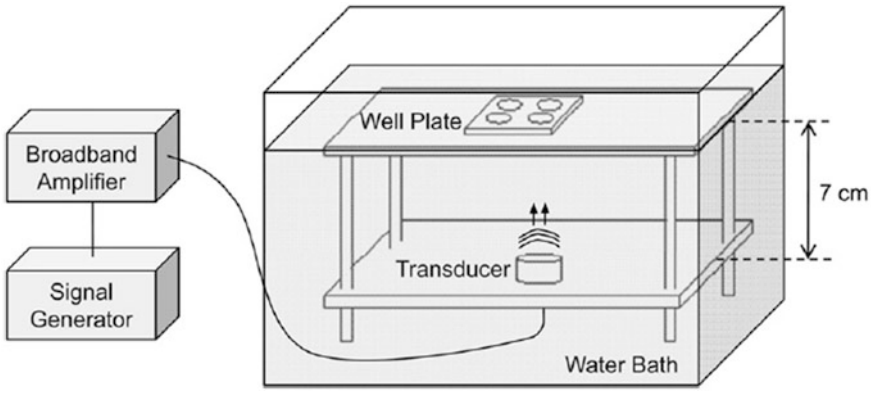

Fig. 2.28 Schematic showing an experimental ultrasound irradiation system

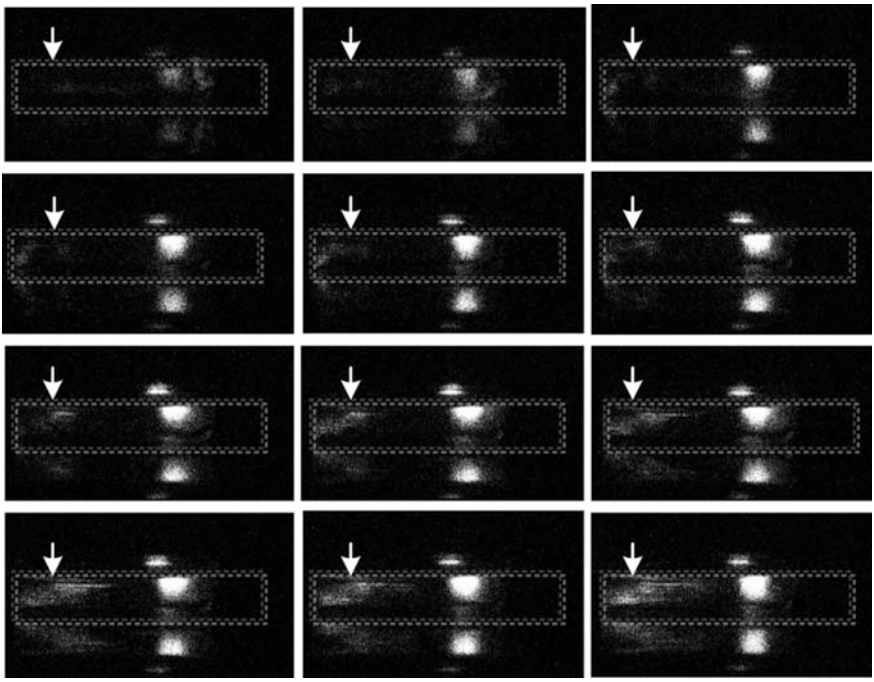

Fig. 2.29 The SCL image of cavitation in the bioreactor

bioreactor represents a new method for mapping the cavitation intensity and distribution. For a bioreactor containing cells, ultrasound irradiation, and microbubbles, studies have shown that microbubbles increase the effect of cavitation on cells. Thus, to illuminate a cavitation map, 10 μL/10 mL lipid-shelled microbubbles were added to a bioreactor system with luminol. As shown in Fig. 2.29, the SCL image sequence was acquired at acoustic power of 15 W. In the dotted rectangle which indicates the edge of bioreactor, the standing wave was developing as time went on. It became prominent and more widely distributed when the lipid-shelled microbubbles were added. This may have occurred because of more cavitation nuclei in the system or a stronger vibration of cavitation.

2.4 ACD, PCD, and Doppler Methods

When a bubble oscillates, acoustic waves are emitted. If the ultrasound power is low, then the bubble simply pulsates in an approximately linear manner emitting signals at the insonation frequency (Leighton 1994). In more powerful acoustic fields, cavitation bubbles may be generated, and the emissions contain both broadband signals and line-spectrum components at specific frequencies.

The line-spectrum components represent the harmonics, ultraharmonics, and subharmonics of the insonation frequency (McLaughlan et al. 2007). Based on the emissions from acoustically driven bubbles, that acoustic methods that can be used to detect cavitation include acoustic scattering, acoustic emission, and Doppler method.

2.4.1 Acoustic Scattering and ACD

When ultrasonic waves impinge on a free-bubble or a gas-filled cavity within a structure, much of the energy is reradiated, i.e., scattered, into the surrounding medium, especially under resonance conditions. Based on this, a system capable of sending and receiving pulses of focused 30-MHz ultrasound (Roy et al. 1990) has been used to detect short-lived cavitation events that result from in vivo exposure of rat lung tissue to four-cycle bursts of focused 4-MHz ultrasound (Holland et al. 1992). This pulser–receiver detection system is known as ACD, and the experimental apparatus is shown in Fig. 2.30. The ACD system can be divided into pulse-echo and bistatic pulse–receiver detections. Transient cavitation can be detected with the acoustic backscattering technique.

ACD can afford sufficient sensitivity and temporal resolution to noninvasively detect the presence of a single 1-μm bubble that lasts only a microsecond (Roy et al. 1990). However, bubble growth can also be produced by therapeutic ultrasound in tissues. Thus, longer interrogating tone bursts have been achieved through bistatic pulser–receiver detection systems. Such systems have been used to investigate shell disruption and fragmentation of biosphere^{TM} and Optison^{TM} ultrasound contrast microbubbles caused by high-amplitude tone bursts (Chen et al. 2002). In another study, Shi et al. (2000, 2001) utilized ACD to investigate the destruction of

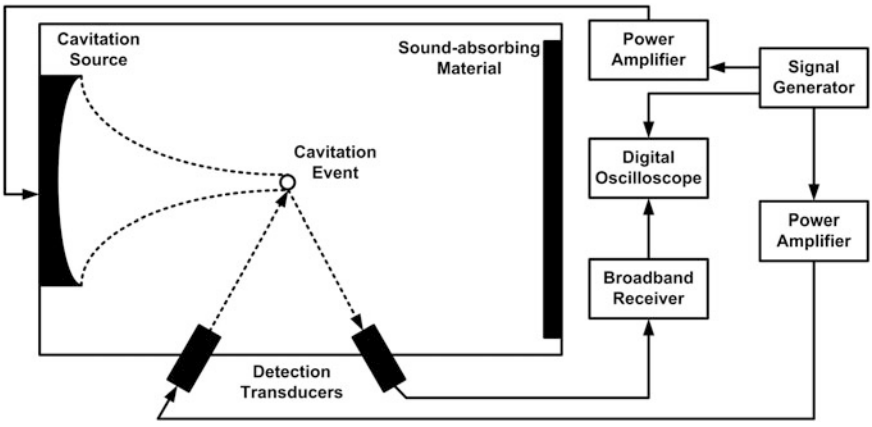

Fig. 2.30 The experimental apparatus for ACD

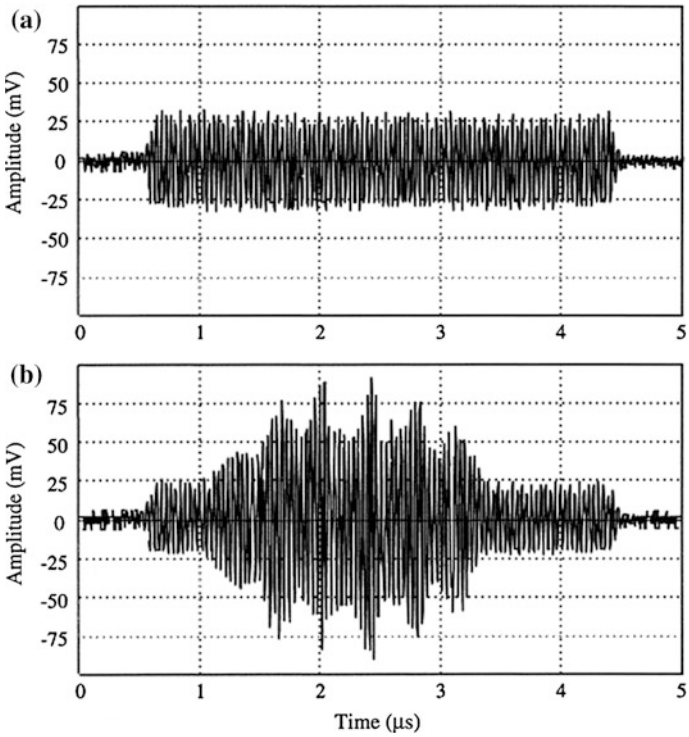

Fig. 2.31 Scattered signals from two single Sonazoid® microbubbles: **a** without exposure to imaging pulses and **b** with insonation by a 2.5-MHz acoustic pulse of 6 cycles and 0.34 MPa. Reproduced with permission from Shi et al. © World Federation for Ultrasound in Medicine and Biology

insonified Sonazoid microbubbles and how this destruction was association with inertial cavitation in vitro. Figure 2.31 shows the results of experimental ACD system, which used real scattered signals from two single Sonazoid microbubbles, without or with exposure to imaging pulses.

In general, ACD can be performed by using a single-element transducer including an unfocused or a focused probe as the pulse-echo detector to actively receive the acoustic backscatter signal generated by cavitation. When an unfocused ACD transducer is employed, the sensitivity may be less. Thus, most experimental studies use focused ACD transducers. Figure 2.32 shows the backscattered signals received by a focused ACD. Since these focused transducers only have a fixed focus, the ACD could only detect cavitation in the focal region, and it could not distinguish between different sources in the region.

Recently, ACM has been developed on the basis of ACD by using a linear array connected to the ultrasound system to increase the spatial coverage for cavitation detection. As one of ACM, conventional B-mode ultrasound imaging has been used to study bubble activity generated by therapeutic ultrasound, lithotripsy, and

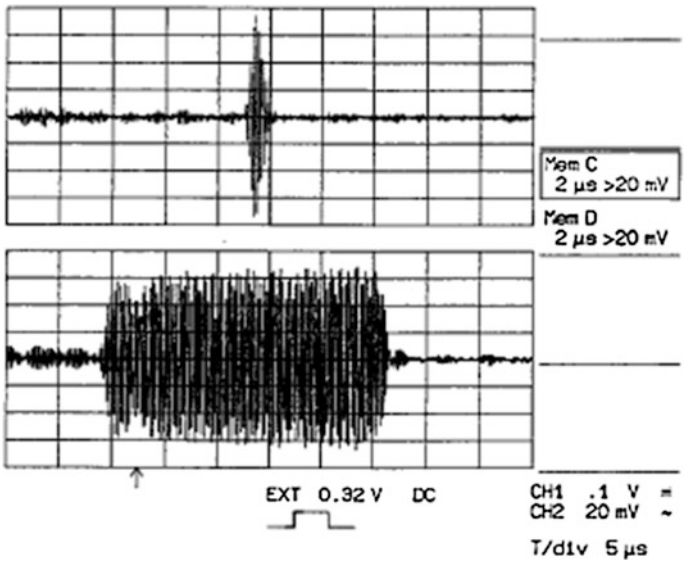

Fig. 2.32 Backscattered signals received by ACD. The *top* trace indicates the presence of a short-lived cavitation event. The bottom trace indicates the presence of an aggregate of polystyrene spheres that persisted in the focal region of the detector for the entire pulse duration (10 µs). The time base for the two traces is 2 µs/div (Crum et al. 1992). Reproduced with permission from Crum et al. © Acoustical Society of America

histotripsy. It is believed that the appearance of a hyperechoic region in ultrasound images results from bubble formation. However, due to a time difference existing between the acquisitions of two scan lines in one frame, strictly simultaneous ACM cannot be achieved. A modified ultrasound line-by-line scanning method for spatial–temporal ACM was proposed by Ding et al. (2013). The details of this method are discussed in Sect. 2.5, and the maps obtained offer high sensitivity and SNR. In addition, because there is a long enough time for the liquid to return to its original state after the acquisition of each scan line, the interactions between the interrogating pulse and bubble behavior are reduced. Therefore, this technique may eventually become standard in cavitation mapping with both high spatial and temporal resolution, similar to exact acoustic field measurements. In another study, Gateau et al. (2011a) reported ultrafast active cavitation imaging using plane wave transmission along the entire aperture of the array at a high frame rate. Figure 2.33 shows the results of ultrafast active cavitation imaging, and they show that cavitation events can be monitored during focused ultrasound treatment. However, because the ultrasound beams are unfocused, the lateral resolution of the ultrafast images may need to be improved. Hu et al. (2015) developed another UACM technique with high spatial–temporal resolution by combining plane wave transmission and adaptive beamforming; the details of this method are given in Sect. 2.6.

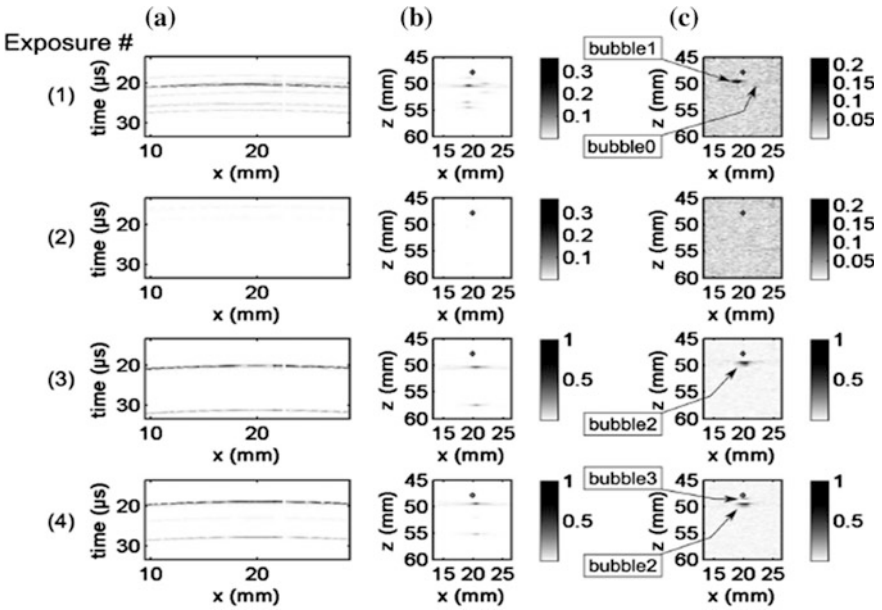

Fig. 2.33 Cavitation imaging using **a** high-pass filtered passive radio frequency data. **b** The corresponding passive beamformed image. **c** The second active change detection image for each shot. Reproduced with permission from Gateau et al. © IEEE

2.4.2 Acoustic Emission and PCD

As we have discussed, cavitation is generally classified into two types: stable cavitation and inertial cavitation. When the acoustic pressure amplitude is low, certain features of the bubble response may be absent under linear conditions. As the acoustic pressure increases, harmonic or subharmonic and ultraharmonic frequency components can be used as indicators of nonlinear bubble motion (Barnett 1998). In general, the resulting emissions at subharmonics and ultraharmonics of the main excitation frequency can be used to reflect stable cavitation. In inertial cavitation, broadband noise emissions appear above the background noise level. These emissions are generated when bubbles undergo large radial oscillations and collapse violently. Atchley et al. (1988) employed an acoustic transducer to passively listen for sound scattered by cavitation microbubbles. This technique, called PCD, relies upon the scattering of the irradiation field by the bubble clouds that arise from cavitation events. Figure 2.34 shows the PCD system, which can be employed to passively detect and monitor cavitation activity by detecting and analyzing the acoustic emissions generated from cavitation events.

Acoustic emissions collected by PCD are sampled digitally and post-processed using one of three signal processing methods, shown in Fig. 2.35. These methods include time-domain, frequency-domain, and time–frequency analysis. The

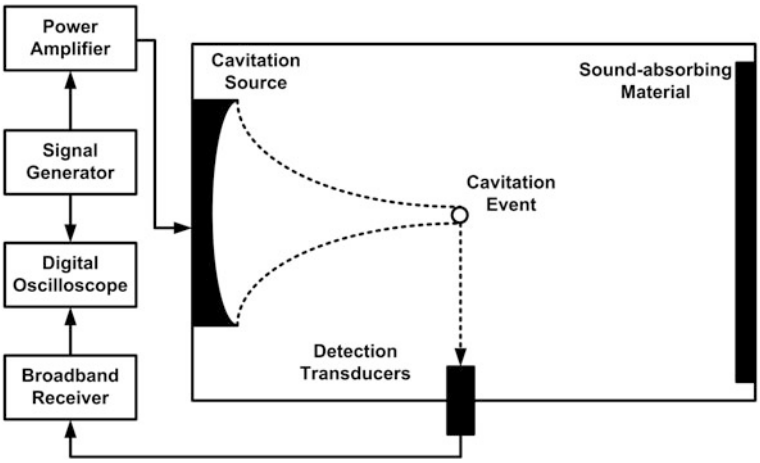

Fig. 2.34 Block diagram of the experimental apparatus for PCD

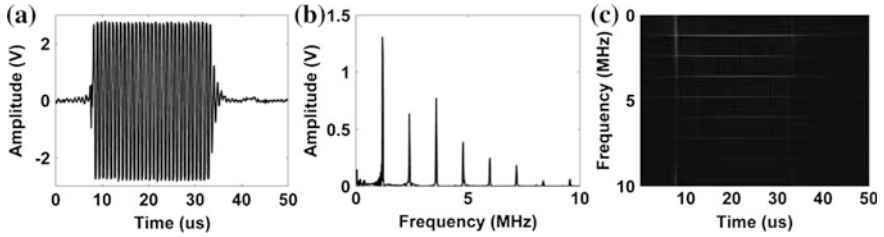

Fig. 2.35 The signal processing methods for PCD signals. **a** Time domain, **b** frequency domain, **c** time–frequency analysis

time-domain analysis is based on the signal waveform, for example, the peak values. The frequency-domain method refers to a spectral analysis of PCD signals performed by fast Fourier transform (FFT). The time–frequency analysis can be achieved by short-time Fourier transformation (STFT). Applying this technique, Ammi et al. (2006) used a time–frequency spectrogram to evaluate the rupture of shelled ultrasonic contrast agents. In another study, time–frequency plots for PCD spectra were generated at three exposure conditions in order to simultaneously compare different signal components (Mast et al. 2007). In such experiments, the changes in the frequency spectra over time can be observed directly from the time–frequency image. However, at present, the frequency-domain method is the most common for analyzing acoustic emissions from PCD signals.

During sonication, the signals generated by cavitation can be grouped into three categories (Leighton 1994; Barnett 1998): (1) The first group consists of the in-sonation fundamental frequency and harmonics that are scattered by particles in the tissue as well as by the stable cavitation and vapor bubbles formed during

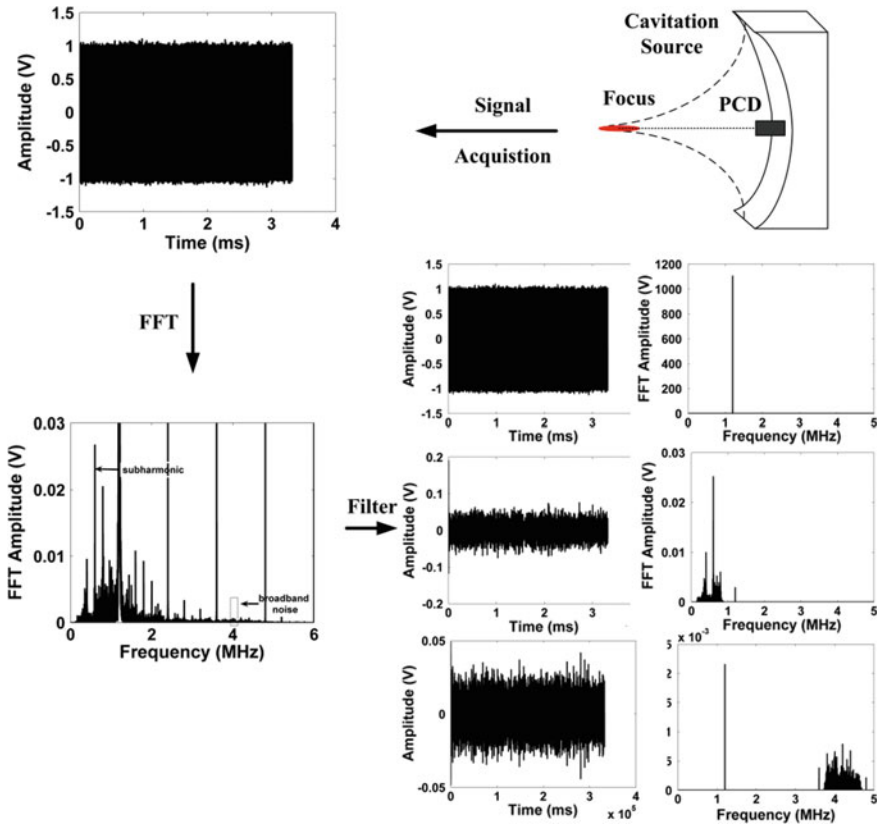

Fig. 2.36 Schematic diagram of PCD signal acquisition and frequency-domain analysis

sonication. Additionally, these signals might include reverberations off other structures present in the tissue, as well as direct propagation of the ultrasound signal. (2) The second group is made up of the subharmonic and ultraharmonic emissions generated from stable cavitation. (3) Finally, the last group contains the broadband acoustic emissions generated by inertial bubble collapses. Figure 2.36 shows the PCD signal acquisition and the frequency-domain analysis. In general, a FFT is performed, in which the signal consists of energy from the scattered sonication signal (fundamental and higher order harmonics), from stable cavitation signals (subharmonics and ultraharmonics), and from the radiated pressure arising from inertial bubble collapses (broadband noise). To isolate the contribution from cavitation, we must remove the fundamental and harmonics by digitally filtering the radio frequency (RF) signals. As such, Farny et al. applied a comb filter around each of the harmonic and ultraharmonic frequencies, so that signal energy only came from the unfiltered frequency gaps between the filtered harmonic and sub-/ultraharmonic peaks, which represented just the energy from inertial cavitation (Farny et al. 2009).

Quantifying the broadband noise in either the time or the frequency domain can allow us to calculate a value called the inertial cavitation dose (ICD), which gives information about the intensity of inertial cavitation (Tu et al. 2006; Chen et al. 2003a). Similarly, by quantifying the subharmonics and ultraharmonics associated with stable cavitation, we can calculate the stable cavitation dose (SCD). Figure 2.37 shows this method of inertial and stable cavitation data acquisition and calculation of the ICD and SCD.

McLaughlan and colleagues (2006, 2007, 2010) identified specific frequencies or frequency ranges of interest after performing an FFT calculation with a Hanning window function. In these studies, the half-harmonic as well as the fourth, fifth, and sixth harmonics plus the broadband frequency was investigated. The fourth harmonic was chosen because it is the first harmonic outside the high-pass frequency band and provided a greater signal strength than the higher harmonics after being transmitted through an attenuating medium, such as ex vivo tissue. In addition to the specific frequencies separated from PCD signals, these studies (McLaughlan et al. 2006, 2007, 2010) also recorded the electrical drive power derived from the measured HIFU drive voltage and audible emissions, and the results are shown in Fig. 2.38.

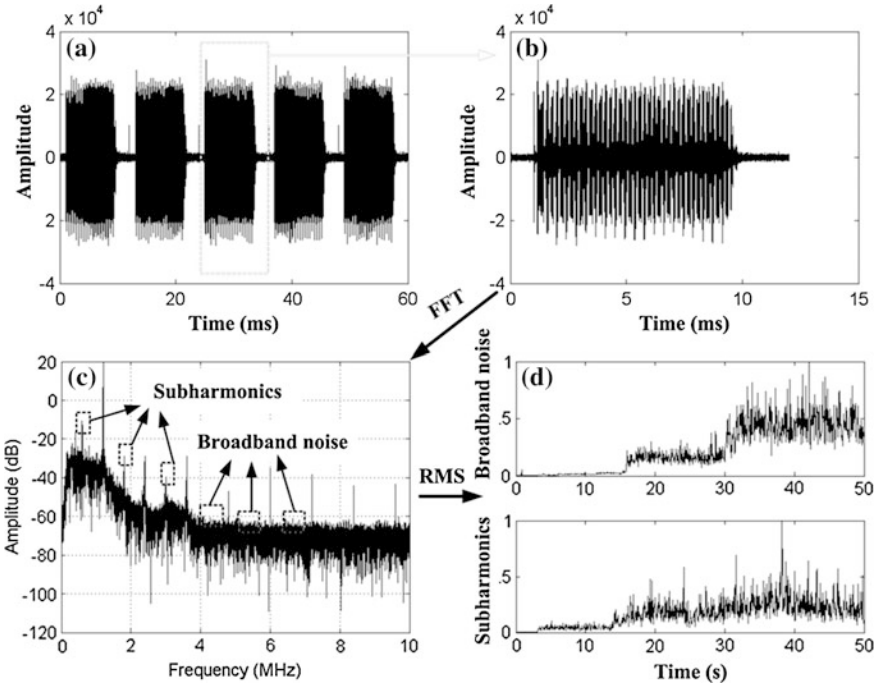

Fig. 2.37 Calculation of the ICD and SCD. **a** Detected cavitation signal from **b** each pulse is converted to **c** its frequency spectrum. The root-mean-square (RMS) amplitude in the broadband noise or in the subharmonic and ultraharmonic regions is measured and plotted in (**d**). Calculation of the ICD and SCD is defined as the integral of the area under the time versus amplitude curve over the 50-s recording

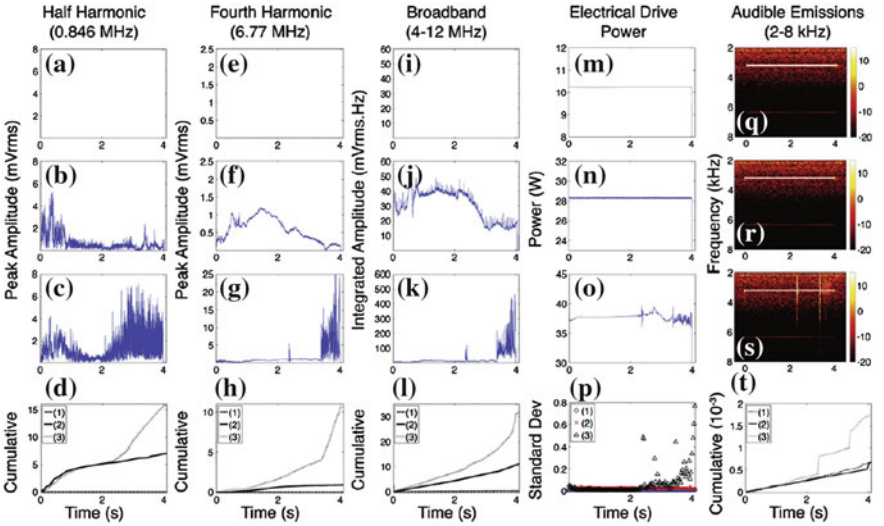

Fig. 2.38 Noise-corrected signals (as labeled) from 4-s HIFU exposures in each of the three cavitation regimes: (*top row*) 314 W/cm^2 (1.52 MPa); (*second row*) 786 W/cm^2 (1.77 MPa); and (*third row*) 1100 W/cm^2 (1.86 MPa). (*Bottom row*) The noise-corrected cumulative signals and standard deviation for the drive power for these three exposures. Reproduced with permission from McLaughlan et al. © World Federation for Ultrasound in Medicine and Biology

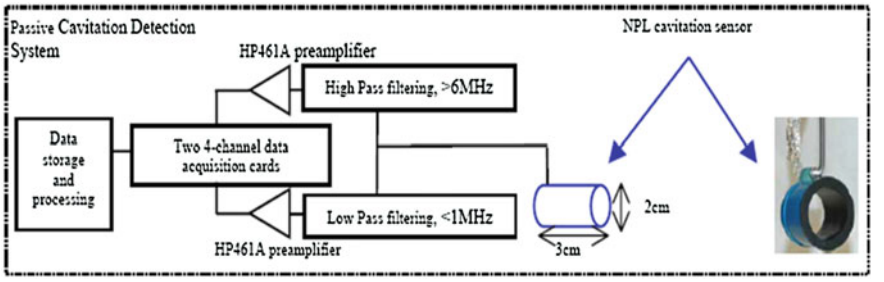

Fig. 2.39 A PCD system, which includes a broadband cavitation sensor. Reproduced with permission from McLaughlan et al. © American Institute of Physics

In order to study bubble activity more effectively, a dual-frequency PCD system, shown in Fig. 2.39, was designed to detect broadband high-frequency emissions (6–12 MHz) generated by acoustic cavitation during HIFU exposures (McLaughlan et al. 2006, 2007). In this system, a high-pass filter and a low-pass filter are used to reduce RF pickup from the drive and acoustic interference. This dual-frequency PCD system allows for the simultaneous investigation of multiple acoustic

emissions, particularly the ultraharmonics, the half-harmonic, and the high-frequency broadband emissions. Furthermore, ACD and PCD can be combined to monitor cavitation dynamics (Everbach and Francis 2000; Gateau et al. 2011a, b). With a combined ACD-PCD system, we can obtain the return echoes of the probe signal by the emitting transducer, and these echoes can be taken as evidence of the presence of microbubbles acting as scatterers. Simultaneously, emissions of broadband noise emanating from the cavitation events are received by a second transducer, and these emissions can be taken as evidence of inertial cavitation. Recently, passive mapping of acoustic cavitation emissions using an ultrasound array has been developed, and it has potential application in real-time monitoring of ultrasound ablation. This will be described in detail in Sect. 2.8.

Unlike the ACD, PCD may not be sensitive enough to detect the occurrence of a weak cavitation event. Thus, the cavitation events detected by PCD are likely to be associated with bubble clouds rather than single bubbles. Generally, PCD is more sensitive to either resonance-sized bubbles or clouds of bubbles. Conversely, ACD using a focused transducer with a high center frequency is more sensitive to single bubbles in the micron size range. Also, the PCD technique yields threshold values lower than those measured via light production, yet higher than theoretical predictions based on free-bubble cavitation models (Roy et al. 1990). Therefore, inertial cavitation may be isolated in real time by using a PCD transducer with a sufficiently high center frequency relative to the insonation frequency, and by applying a high-pass filter to remove the energy at the first few insonation harmonics.

2.4.3 Frequency Shift Signal and Doppler

Rapid bubble growth and collapse, as occurs in cavitation, can generate a frequency shift signal that exhibits the Doppler effect (Deng et al. 1996). Thus, Doppler can be used to detect cavitation using a system such as that shown in Fig. 2.40. Using this system, cavitation was detected by a modified version of an active cavitation detector, which employed a highly focused transducer with center frequency of 30 MHz. An oscilloscope was used to monitor and record the post-processed signal received by the detection transducer. Also, a trigger level was set so that only signals of substantially higher voltage than the general background noise would be recorded and recognized as a cavitation event.

In this setup, the backscattered signal is displayed and recorded on the oscilloscope as time traces. These traces, which are the scattered signals from cavitation bubbles, are modulated both in amplitude and in frequency due to the movement of the bubble wall. Using a double balanced RF/IF mixer and a low-pass filter, frequency demodulation is achieved. The output signal from the demodulation scheme

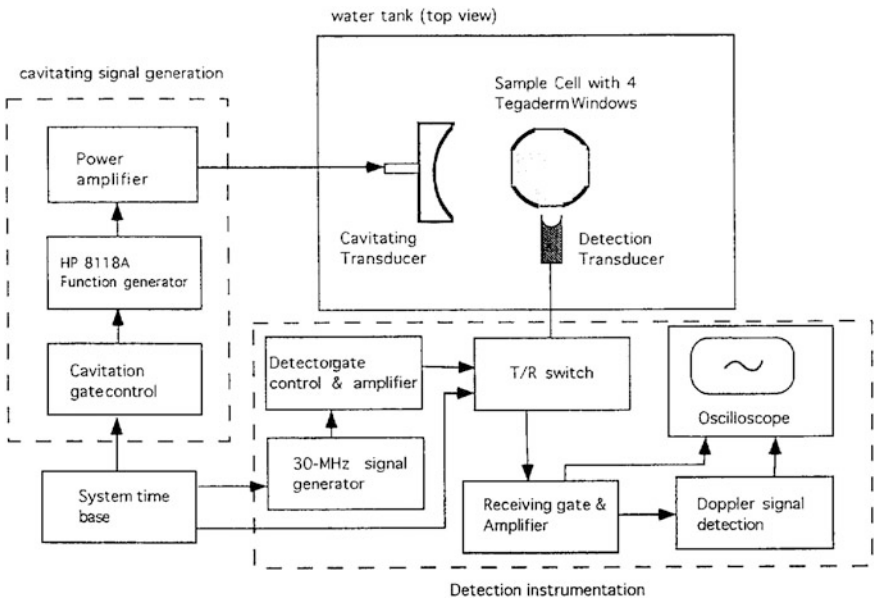

Fig. 2.40 Typical cavitation events recorded in blood showing a broadened bubble movement. *Bottom* trace is in the time trace, and the *top* trace is the Doppler frequency shift signal. Reproduced with permission from Deng et al. © World Federation for Ultrasound in Medicine and Biology

represents the frequency shift of the scattered signal from the original probing signal. The frequency shift signal obtained in this way is also displayed along with the time trace on the oscilloscope. A typical recording of a cavitation event in plasma is shown in Fig. 2.41. The Doppler frequency shift range is up to 1.5 MHz, which is much higher than that caused by the translation motion of a solid particle.

These cavitation events were also recorded in blood, and the results are shown in Fig. 2.42. The Doppler frequency shift signal showed broadened bubble movement. Based on this, a cavitation event could be distinguished from a solid particle. The backscattered signals from cavitation in these blood samples were different from those in water or plasma. Compared to the multiple growth and collapse events that occurred within one pulse in water or plasma (Fig. 2.41), the signals in blood showed that only one or two cycles of growth and collapse occurred, and the cycles were somewhat broader, as demonstrated in Fig. 2.42.

The frequency detection scheme described above has been tested using simulated signals and is advantageous in situations when noise or a large reflection is present. If the time trace shows a large reflection from a solid particle in the host medium, any scattering from a cavitation bubble may be obscured by the large reflection. Therefore, the time trace will not demonstrate the characteristic rapid

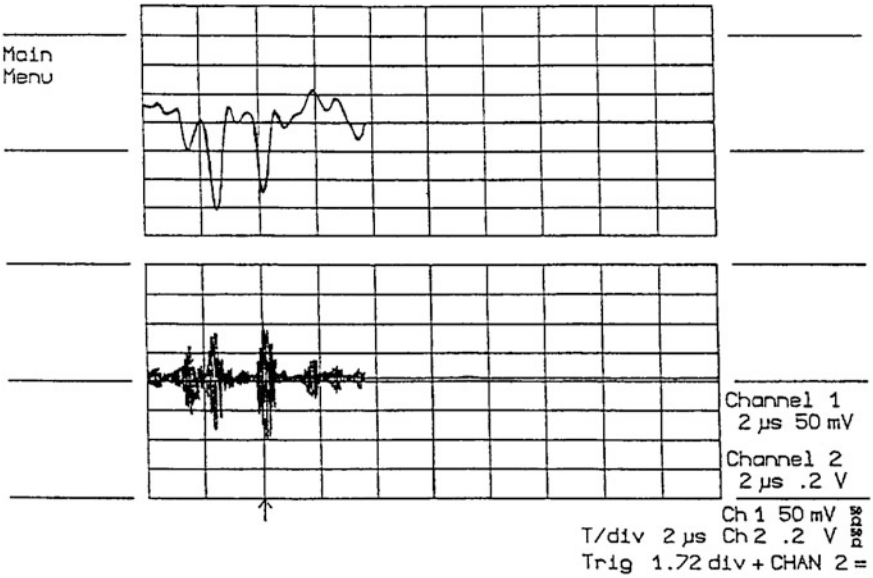

Fig. 2.41 Typical cavitation events recorded in plasma showing a distinguishable bubble and collapse. *Bottom* trace is in the time trace, and the *top* trace is the Doppler frequency shift signal. Reproduced with permission from Deng et al. © World Federation for Ultrasound in Medicine and Biology

oscillation behavior of a cavitation bubble. However, the frequency shift signal will exhibit the Doppler effect of rapid bubble growth and collapse, from which a cavitation event can be distinguished from a solid particle.

Recently, a new method for detecting cavitation has been developed, and it is based on the "twinkling" artifact (TA) of Doppler imaging (Khokhlova et al. 2013). TA that can be explained by irregular scattering of the Doppler ensemble pulses from the fluctuating microbubbles is used to detect cavitation in tissue and in polyacrylamide gel phantoms during pulsed 1-MHz HIFU exposures with different peak negative pressures (PNPs) (1.5–11 MPa). Besides, Li et al. proposed a bubble Doppler method based on a fusion of the three Doppler techniques—color Doppler, pulse-inversion Doppler, and interleaving Doppler (Li et al. 2014). These techniques were found to be not only more sensitive than conventional PCD or high-speed photography, but also complementary to each other, providing different information about the bubble distribution. With bubble Doppler, a cavitation event is considered to have occurred if color was displayed on top of the B-mode image. The details of this method are given in Sect. 7.5.

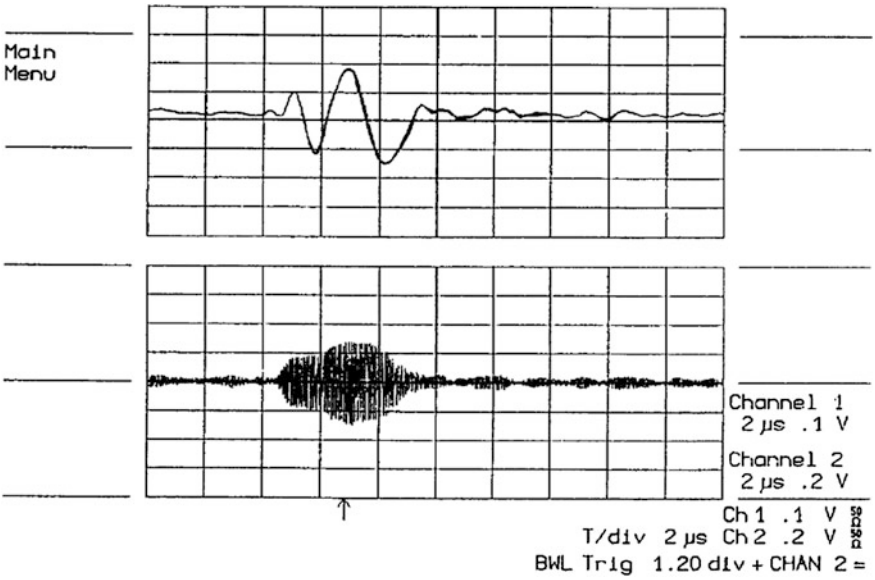

Fig. 2.42 Typical cavitation events recorded in blood showing broadened bubble movement. *Bottom* trace is in the time trace, and the *top* trace is the Doppler frequency shift signal. Reproduced with permission from Deng et al. © World Federation for Ultrasound in Medicine and Biology

2.5 Precise Active Acoustic Mapping of Cavitation Bubbles

2.5.1 Ultrasound Line-by-Line Scanning Method

As cavitation is highly complex and exhibits transient characteristics, it is essential to develop a standard cavitation mapping technique similar to exact acoustic field measurements, with both high spatial and temporal resolution. A precise active acoustic mapping of cavitation bubbles by a modified ultrasound line-by-line scanning method is proposed by Ding et al. (2013). Scattered signals from cavitation bubbles are obtained in a scan line immediately after one HIFU exposure, and then, there is a waiting between the next exposure to allow the liquid to return to its original state. As this pattern is extended, an image can be built up by sequentially measuring a series of such lines.

A linear array driven by an ultrasound scanner (Sonix-RP) was used to perform precise ACI. The input signal configuration was a line trigger. The synchronization of the HIFU exposure and RF data acquisition by the Sonix-RP scanner are illustrated in Fig. 2.43. The HIFU exposure time (T) and time delay (D) between the Sonix-RP triggering pulse and the moment when the HIFU is turned off varied from

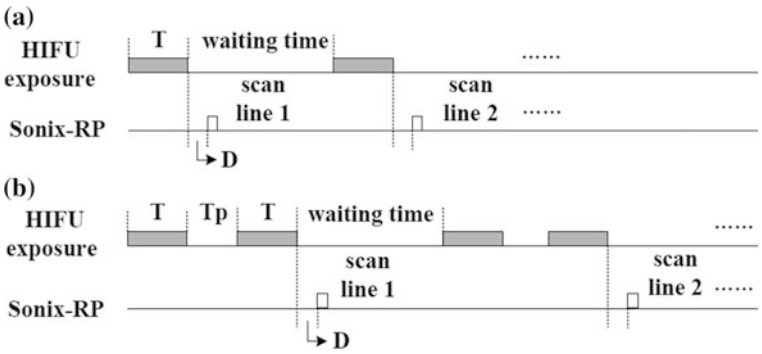

Fig. 2.43 Timing sequences for the modified ultrasound line-by-line scanning method. **a** Timing sequence used to investigate the temporal evolution of the cavitation bubble cloud and the dissolving process of corresponding bubbles, which was done by varying the parameters T and D, respectively. **b** Timing sequence used to investigate the spatial distribution affected by the previously generated cavitation, which was done by changing the parameters T or T_p. Reproduced with permission from Ding et al. © Elsevier

microseconds to seconds. Evolution of cavitation bubble cloud and its dissolution are acquired through varying the parameters T and D in Fig. 2.43a, respectively. In Fig. 2.43b, T_p is the interval between two HIFU exposures called pulse pairs, which consisted of the previous pulse and the next pulse. By changing the parameters T or T_p, as in Fig. 2.43b, the spatial distribution affected by the previously generated cavitation was investigated.

2.5.2 *Repeatability and Feasibility*

The line-by-line scanning method would strictly only be valid when the cavitation distribution is repeatable, such as when all conditions, including HIFU output and the physical properties of the surrounding medium, are the same. Because the generation of a cavitation event always accompanies with randomness, a cavitation cloud is unlikely to be perfectly reproduced. However, on the broad scale of mapping bubble clouds, building up a cavitation map using the line-by-line method may be valid, and we show the results of reproducibility tests, in which specific test cases were remeasured. For each pf the specific test cases, 20 measurements were taken. The time interval between measurements was about 5 min, and no insonation occurred in the time interval. Figure 2.44 shows the results of this remeasuring on three different timescales. Here, we can see that the initial results for the first scan line could be almost reproduced at the end. Also, the two cavitation maps obtained using the line-by-line scanning method in tap water appeared very similar. These results may prove the broadscale repeatability of this method for cavitation mapping.

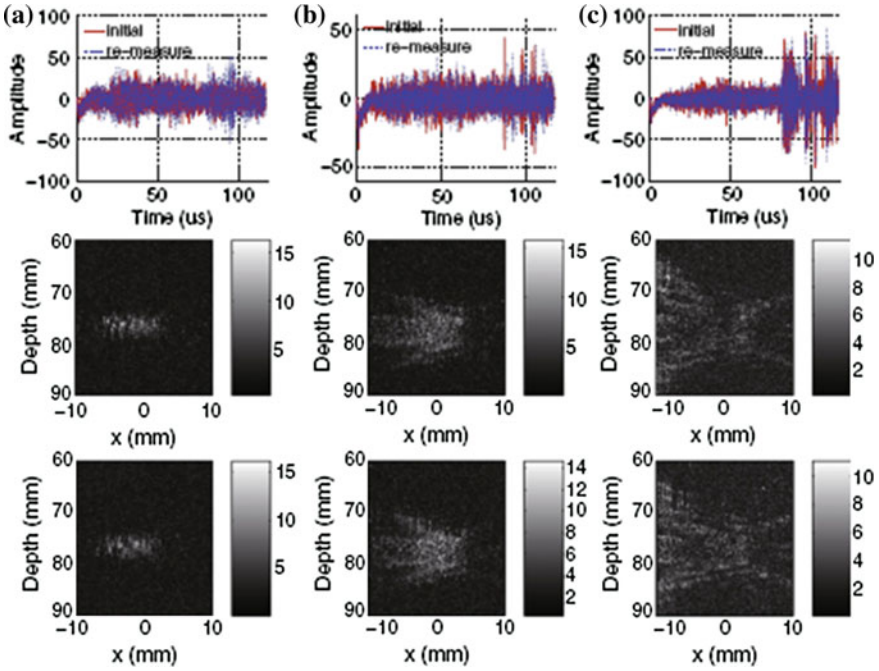

Fig. 2.44 Results of remeasuring specific test conditions on three different timescales. The exposure times of the FUS in (**a**–**c**) are 50 μs, 5 ms, and 30 ms, respectively. The first row shows the RF signal of the first scan line for both the initial and the remeasured experiments. The second and third rows illustrate two cavitation maps in tap water obtained by the ultrasound line-by-line scanning method. Reproduced with permission from Ding et al. © Elsevier

2.5.3 Spatial and Temporal Cavitation Distributions

The temporal evolution of a cavitation bubble cloud in tap water is shown in Fig. 2.45. Due to the highest acoustic pressure, the bubble cloud first emerged in the focal region. Later, the cavitation bubbles expanded symmetrically because inertial cavitation generated more bubbles, nucleating additional cavitation activity. The cavitation bubble cloud subsequently grew forward into the post-focal region, moving along a specific path and thus forming "streamers" like a tree crown, which are determined by the distribution of acoustic pressure. Bubbles in the post-focal and focal region can reflect ultrasound energy, causing cavitation bubbles to appear in the prefocal region with a separate branch structure. These results are consistent with those of previous studies (Chen et al. 2006b). When T was increased to 200 ms, the streaming due to acoustic radiation became bigger and the bubbles were pushed farther upward. Also, the prefocal region had the secondary maximum acoustic intensity, especially where close to focal region. Thus, in the prefocal region, bubbles (pointer in Fig. 2.45l) came to dynamic equilibrium. These results

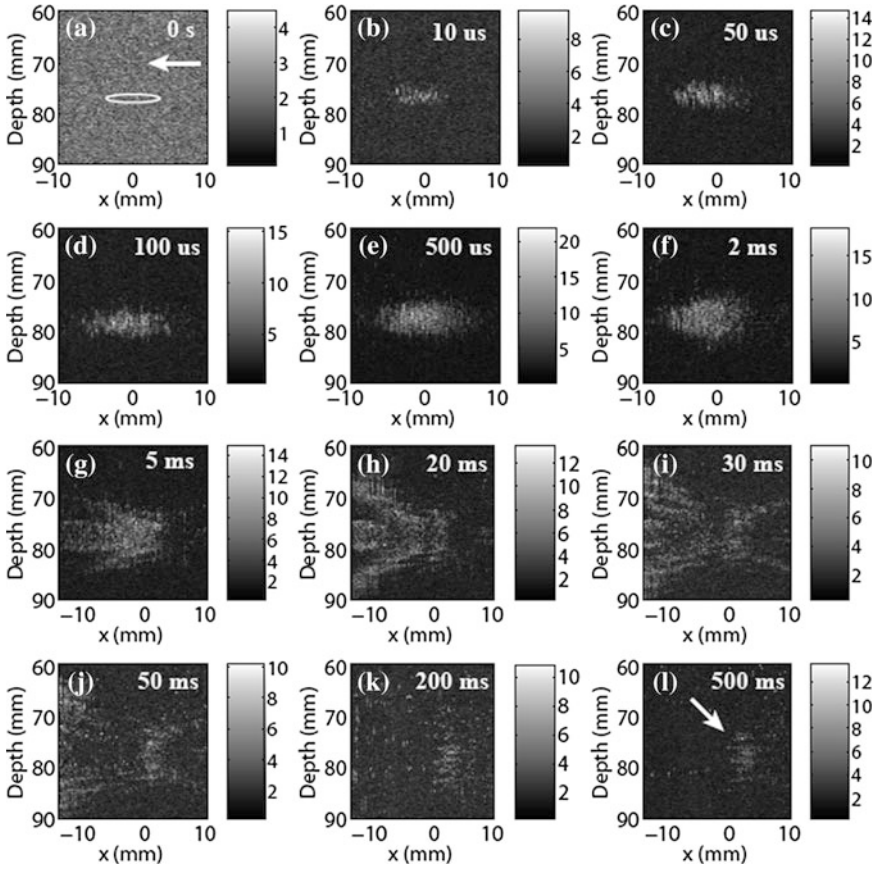

Fig. 2.45 Temporal evolution of the cavitation bubble cloud in tap water. The pointer and the *solid line* in **a** show the transmission direction of HIFU and the position of the focal region, respectively. Bubbles generated in the prefocal region near the focus are pointed out in (**l**). *D* is set to 1.000 ms for the travel time of the sound wave from the HIFU source to the focal region. The various *T* values are indicated in the *right* corner of each image. The zero of the *x*-axis is set to the center element of the array. Reproduced with permission from Ding et al. © Elsevier

suggest that a stable bubble cloud may be created when the parameters of ultrasound exposure are appropriately chosen.

Figure 2.46 shows the temporal evolution of a cavitation bubble cloud in a tap-water-filled spherical cavity in an gelatin–agar phantom. When no HIFU exposure was performed, the map acquired consisted only of the background (Fig. 2.46a). The results of cavitation mapping in the gelatin–agar phantom were obtained by subtracting the background from the cavitation maps. As shown in Fig. 2.46, the cavitation bubble cloud first emerged in the focal region with a high population density. Then, the cloud grew backward into the prefocal region, forming a triangular shape containing the accumulated bubbles. The reason for the

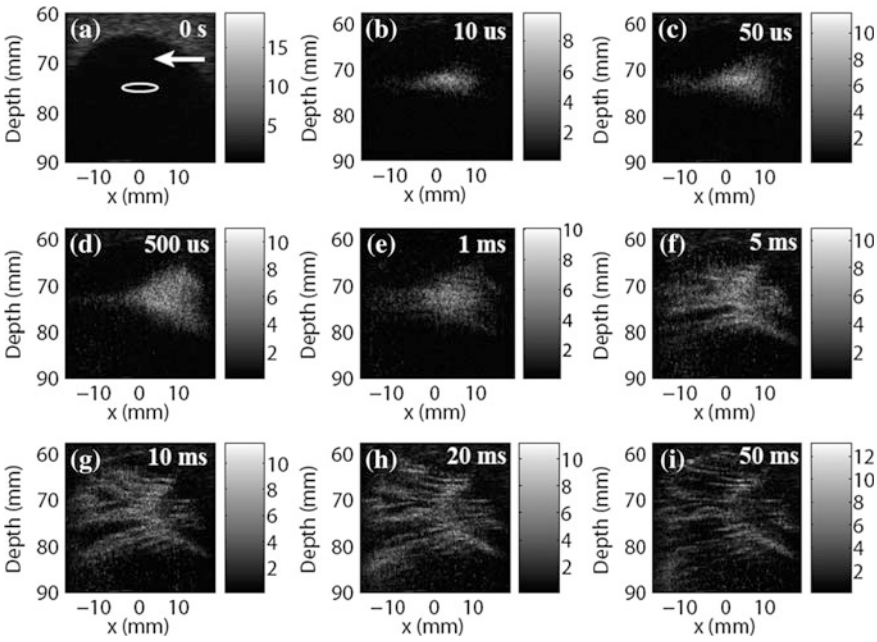

Fig. 2.46 Temporal evolution of the cavitation bubble cloud in a spherical cavity filled with tap water in a gelatin–agar phantom. The pointer and the *solid line* in **a** show the transmission direction of HIFU and the position of the focal region, respectively. *D* was set to 1.000 ms for the travel time of the sound wave from the HIFU source to the focal region. The various *T* values are indicated in the *right* corner of each image. The zero of the *x*-axis was set to the center element of the array. Reproduced with permission from Ding et al. © Elsevier

triangle shape formed is that dense bubbles in the focal region may affect the incident sound field by shielding. When *T* increased to 5 ms, the longer exposure to acoustic radiation caused the bubbles to travel to the post-focal region in a ribbonlike structure. Then, the ribbonlike structure enlarged, and bubbles were generated in almost the entire area of the cavity.

Compared with Fig. 2.45, the formation of the cloud structure in Fig. 2.46 occurred differently. Since the liquid in the cavity was also tap water, the cavitation thresholds were almost the same. However, in the phantom cavity, gas within the bubbles dissolved into the surrounding tap water, increasing the number of cavitation nuclei. Therefore, although the attenuation of the phantom existed, more bubbles were generated in the cavity. In addition, the cloud structure was relatively stable because acoustic radiation forces in the cavity may have been less than those in tap water alone.

The requirement for the cavitation distribution to be repeatable when all the experimental conditions are the same will limit the application of the line-by-line scanning technique to certain media whereby nuclei can be refreshed through movement. Also, the length of time needed to acquire a frame using this method is

quite long (minimum of 128 s). However, because the method uses a focused beam, these maps (as opposed to those produced using plane wave techniques) can give good details with a high lateral resolution of 0.5 mm and an axial resolution of 0.29 mm. Furthermore, using hardware controls, the temporal resolution can reach the submicrosecond level. Also, because there is a long wait time after each scan line is acquired, the interactions between the interrogating pulse and bubble behavior are reduced. Therefore, this technique can be a useful tool to spatially and temporally study cavitation in some cases, providing a reference for clinical HIFU therapy. With more improvement, this technique may develop as a standard tool for cavitation mapping, as it offers both high spatial and temporal resolution.

2.6 Ultrafast Active Cavitation Mapping with a Plane Wave Beam

As described in Sects. 2.2, 2.3, 2.4, and 2.5, cavitation detection methods commonly include high-speed photography (Lauterborn and Ohl 1997; Chen et al. 2006b), SL/SCL (Gaitan et al. 1992; Brenner et al. 2002; Cao et al. 2012) and acoustic methods (Roy et al. 1990; Chen et al. 2003b; Vaezy et al. 2001b; Rabkin et al. 2005; Ding et al. 2013). High-speed photography (Lauterborn and Ohl 1997) can provide the distribution of cavitation bubbles intuitively with high temporal resolution (∼nanosecond), but it demands transparency of the medium. SL and SCL (Cao et al. 2012) can map "active" cavitation bubbles, but these methods also require a transparent medium and their temporal resolution is low because of the weak luminous intensity.

Compared to high-seed photography and SL or SCL, acoustic methods are more suitable for in situ studies. PCD (Atchley et al. 1988; Chen et al. 2003a) and ACD (Roy et al. 1990; Chen et al. 2003b) are two common one-dimensional acoustic detection methods with high sensitivity, but they cannot reflect the spatial distribution of cavitation. ACM (Vaezy et al. 2005; Rabkin et al. 2005) has been developed on the basis of ACD and mainly refers to B-mode imaging. This technique achieves quasi-real-time mapping determined by the line-by-line scan process, and its imaging frame rate is limited, so it cannot capture transient cavitation bubble behavior. Ding et al. (2013) proposed a modified line-by-line scanning ACM (Sect. 2.5) to map cavitation bubbles with high sensitivity and high spatial–temporal resolution, but it is also time consuming and requires repeatable cavitation distributions within a medium.

However, cavitation mapping should be achieved with a high frame rate, preferably at one time over the entire region, because of the transient behaviors of the bubbles. Gateau et al. (2011a, b) have proposed a plane wave-based UACM, and they combined it with passive detection to detect and locate the cavitation events both in vitro and in vivo and performed a tilted plane wave compounding to improve the imaging quality and detection sensitivity. As reported in another study,

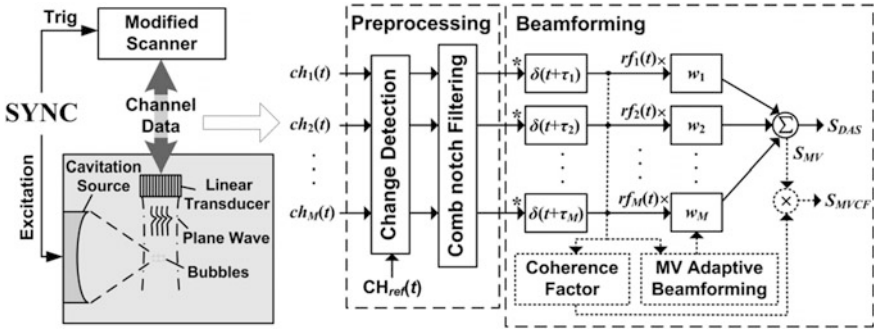

Fig. 2.47 Schematic representation of UACM

however, Hu et al. (2015) developed a UACM with high spatial–temporal resolution by combining plane wave transmission and adaptive beamforming to monitor the evolution of residual cavitation bubbles in histotripsy.

In this technique, the UACM with a plane wave beam is performed on a modified ultrasound scanner, which is accessible to channel-domain radio frequency (RF) data. A schematic of the method is shown in Fig. 2.47. The received channel-domain raw RF data are first preprocessed as follows: (1) A change detection is performed to suppress the background backscatter signal and extract the cavitation bubble signal; (2) a comb notch filter is applied to filter out the fundamental and harmonic HIFU frequencies to eliminate the strong interference from the HIFU field. After these preprocessing steps, a beamforming algorithm is then applied to form the final cavitation bubble images. According to the different beamforming algorithms, the plane wave UACM can be divided into plane wave delay-and-sum (DAS)-based UACM and plane wave adaptive beamforming-based UACM (Hu et al. 2015).

2.6.1 Plane Wave DAS-Based UACM

DAS is a conventional time-domain beamformer that uses a fixed set of time delays and aperture weightings to combine the channel-domain signals from the elements in the array. Time delays, adjusted for every depth on image formation to achieve dynamic receive focusing, are calculated as the propagation time from the transmitting element to the focus point and back to the receiving element, as shown in Fig. 2.48. Assuming an active aperture of M elements for a given point $\vec{r}_p$, the time delay for the mth element signal is given by:

$$\tau_m(\vec{r}_p) = \frac{\left\|\vec{r}^{\,\mathrm{xmt}} - \vec{r}_p\right\| + \left\|\vec{r}^{\,\mathrm{rcv}} - \vec{r}_p\right\|}{c} = (z + \sqrt{z^2 + (x - x_m)^2})/c \qquad (2.1)$$

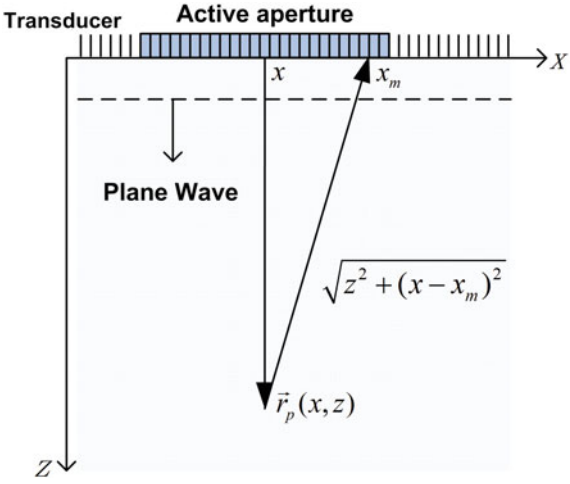

Fig. 2.48 Time delays for a plane wave insonation

for $m = 0, 1, \ldots, M-1$, where c is the speed of sound, and $\vec{r}^{\text{xmt}}$ and $\vec{r}^{\text{rcv}}$ are the spatial positions of the transmitting and receiving elements, respectively.

Then, the mth delayed element signal is given by:

$$\text{rf}_m(t) = \text{ch}_m(t + \tau_m(\vec{r}_p)) \tag{2.2}$$

where $\text{ch}_m(t)$ is the received channel-domain raw RF signal on the mth element.

Given a fixed aperture weighting, the delayed element signals are then weighted and summed as follows:

$$S_{\text{DAS}}(t) = \sum_{m=1}^{M} w_m(t)\text{rf}_m(t) = \mathbf{w}(t)^{\text{H}}\mathbf{RF}(t) \tag{2.3}$$

where $w_m(t)$ is the aperture weighting for element m, $\mathbf{w}(t) = [w_1(t)w_2(t)\cdots w_M(t)]^{\text{T}}$, $\mathbf{RF}(t) = [\text{rf}_1(t)\text{rf}_2(t)\cdots\text{rf}_M(t)]^{\text{T}}$, and $(\cdot)^{\text{H}}$ and $(\cdot)^{\text{T}}$ denote the conjugate transpose and transpose, respectively. The beamformed RF data are then enveloped and scaled to form UACM images.

2.6.2 Plane Wave Adaptive Beamforming-Based UACM

Adaptive beamforming calculates element weightings adaptively to the input signals to reduce the main lobe and depress the side lobes. This technique differs from conventional DAS beamforming, which uses fixed weightings. The widely used adaptive beamforming algorithm is the MV beamforming proposed by Capon (1969), of which the basic idea is to make noise as well as the signal from

non-interference directions contributes minimally to the signal power while keeping the signal power from source direction constant. MV beamforming was initially used in radar, radio communications, and other far-field, non-correlated narrowband signal areas. In recent years, it has begun to be applied to near-field, highly correlated broadband ultrasound imaging (Wang et al. 2005; Asl and Mahloojifar 2009; Synnevag et al. 2007). Also, spatial smoothing and diagonal loading have been introduced to remove the strong correlation of ultrasonic signals and improve the robustness of the algorithm (Synnevag et al. 2007). CF weighting (Asl and Mahloojifar 2009) is another adaptive side lobe reduction method that works through weighting the image pixel by the corresponding CF (Asl and Mahloojifar 2009), in which the CF (Hollman et al. 1999) is initially used as a focusing index to indicate the focusing quality. Hu et al. (2015) combined plane wave transmission, MV beamforming, and CF weighting to achieve a plane wave MVCF-based UACM, as a representative of adaptive beamforming-based UACM, to image cavitation bubbles with a high SNR and high spatial–temporal resolution.

In plane wave DAS-based UACM, the aperture weightings are predefined and fixed, whereas MV beamforming uses the recorded signal to compute the weights adaptively by minimizing the variance of the beamformed output while maintaining a distortionless response of the focal point. This optimization problem can be formulated as follows (Cox et al. 1987):

$$\min_{\mathbf{w}(t)} \mathbf{w}(t)^{\mathrm{H}}\mathbf{R}(t)\mathbf{w}(t), \quad \text{subject to } \mathbf{w}(t)^{\mathrm{H}}\mathbf{a} = 1 \tag{2.4}$$

where $\mathbf{R}(t)$ is the covariance matrix of $\mathbf{RF}(t)$ and $\mathbf{a}$ is the steering vector. Due to time delaying, $\mathbf{a}$ is simply a vector of ones. The solution to Eq. (2.4) is given by Cox (1987):

$$\mathbf{w}_{\mathrm{opt}}(t) = \frac{\mathbf{R}(t)^{-1}\mathbf{a}}{\mathbf{a}^{\mathrm{H}}\mathbf{R}(t)^{-1}\mathbf{a}} \tag{2.5}$$

Spatial smoothing (Synnevag et al. 2007) is used to decorrelate the coherent received signals by dividing the array into overlapping subarrays followed by averaging the covariance matrices for all subarrays. With spatial smoothing, the covariance matrix is estimated as follows (Synnevag et al. 2007):

$$\widehat{\mathbf{R}}(t) = \frac{1}{M-L+1}\sum_{l=1}^{M-L+1} \mathbf{RF}_l(t)\mathbf{RF}_l(t)^{\mathrm{H}} \tag{2.6}$$

where L is the subarray length, and $\mathbf{RF}_l(t) = [\mathrm{rf}_l(t)\mathrm{rf}_{l+1}(t)\cdots\mathrm{rf}_{l+L-1}(t)]^{\mathrm{T}}$ is the delayed element vector for the lth subarray.

Diagonal loading (Synnevag et al. 2007) has also been introduced to improve the robustness of MV beamforming by adding a constant to the diagonal of the covariance matrix, replacing $\widehat{\mathbf{R}}(t)$ with $\widehat{\mathbf{R}}(t) + \varepsilon\mathbf{I}$. Here, ε is set to Δ times of the

power in the received signals, **I** is the diagonal identity matrix (Synnevag et al. 2007):

$$\varepsilon = \Delta \cdot \mathrm{trace}\left\{\widehat{\mathbf{R}}(t)\right\} \tag{2.7}$$

The MV beamformed output is then given by:

$$S_{MV}(t) = \frac{1}{M-L+1}\sum_{l=1}^{M-L+1} \mathbf{w}_{\mathrm{opt}}(t)^{\mathrm{H}}\mathbf{RF}_l(t) \tag{2.8}$$

CF weighting is defined as the ratio between the energy of the coherent sum to the total incoherent energy (Hollman et al. 1999):

$$\mathrm{CF}(t) = \frac{\left|\sum_{m=1}^{M}\mathbf{RF}(t)\right|^2}{M\sum_{m=1}^{M}|\mathbf{RF}(t)|^2} \tag{2.9}$$

The final output of MVCF-based UACM is given by:

$$S_{\mathrm{MVCF}}(t) = S_{\mathrm{MV}}(t)\cdot \mathrm{CF}(t) = \frac{\mathrm{CF}(t)}{M-L+1}\sum_{l=1}^{M-L+1}\mathbf{w}_{\mathrm{opt}}(t)^{\mathrm{H}}\mathbf{RF}_l(t) \tag{2.10}$$

The beamformed RF data are then enveloped and scaled to form UACM images.

2.6.3 Performance of UACM in a Free Field

A focused single-element concave transducer (Imasonic, Besancon, France) driven by a double-channel arbitrary waveform generator (AWG420, Tektronix) with sine wave through a power amplifier (AG1017, T&G Power Conversion, Inc., Rochester, NY) was used as the energy source to generate cavitation in free field. A SonixTOUCH ultrasound scanner (Ultrasonix Medical Corp., Richmond, BC, Canada), equipped with a 128-element linear transducer array (L14-5/38 probe, center frequency of 7.5 MHz, 65 % bandwidth) and a plug-in module for parallel data acquisition of the raw ultrasound data (SonixDAQ, Ultrasonix Medical Corp., Richmond, BC, Canada), was used to perform UACM by programmable plane wave transmission (5 MHz, 1 cycle). The 128-element linear transducer array was aligned with the HIFU focus confocally. The time delay between cavitation excitation and UACM was 1 ms, and the sampling rate of UACM was 40 MHz.

The performances of UACMs were evaluated using the level of the SNR and the resolution. Figure 2.49 illustrates the comparison among conventional B-mode

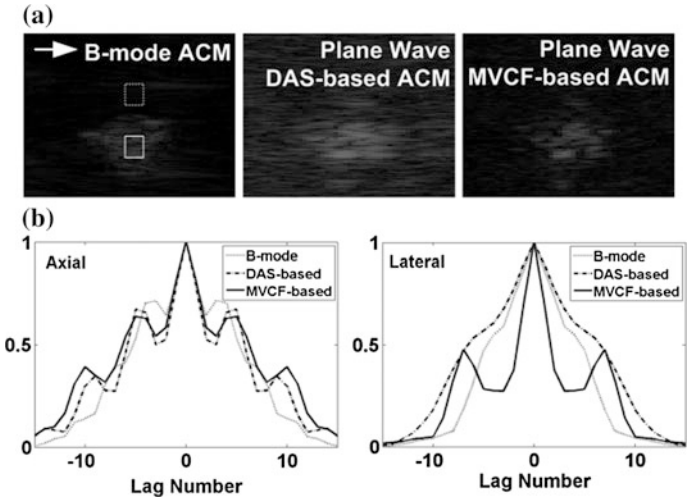

Fig. 2.49 Comparing conventional B-mode ACM, plane wave DAS-based UACM, and plane wave MVCF-based UACM in a free field. The dynamic range was 40 dB for all images (15 mm × 15 mm in dimension), and the rectangular boxes were used to calculate the SNR. Reproduced with permission from Hu et al. © Acoustical Society of America

ACM, plane wave DAS-based UACM, and plane wave MVCF-based UACM. The SNRs (defined as $10\lg(P_{\text{signal}}/P_{\text{noise}})$, where P_{signal} and P_{noise} are the power of signal and the noise, respectively) were calculated to be 19.7 ± 1.8, 11.4 ± 2.1, and 20.6 ± 2.9 dB for B-mode ACM, plane wave DAS-based UACM, and plane wave MVCF-based UACM, respectively, in five repeated experiments. From these results, we see that the SNR of the plane wave MVCF-based UACM was 9.2 ± 0.8 dB larger than that of plane wave DAS-based UACM, while it was almost the same as that of B-mode ACM. To quantify the resolution, the −6 dB auto-correlation lengths of the enveloped RF data corresponding to the images were calculated (Abeyratne et al. 1995). The axial resolution of plane wave MVCF-based UACM was 1.6 ± 0.6 times higher than that of DAS-based UACM, and it was 1.3 ± 0.7 times higher than B-mode ACM. Similarly, the lateral resolution of plane wave MVCF-based UACM was 2.4 ± 1.4 times larger than DAS-based UACM and 2.3 ± 1.3 times larger than B-mode ACM (Hu et al. 2015).

The effects of plane wave MVCF-based UACM on bubble behavior have also been studied by detecting the dissipation of cavitation bubbles in water under different UACM parameters. The UACM image sequences of bubble dissipation were quantified to integrate bubble intensities changing with time. The average results for three repeated experiments are illustrated in Fig. 2.50, from which we can see that the dissipation rate decreases as the PNP decreases, and it increases as the frame rate increases. The effect of UACM on bubble behavior is small when the imaging PNP is low. The averaged SNRs of the bubble images under different PNPs were also calculated to be 20.3 ± 1.9, 17.6 ± 0.8, and 13.6 ± 0.9 dB corresponding to PNPs of 240, 160, and 80 kPa, respectively (Hu et al. 2015).

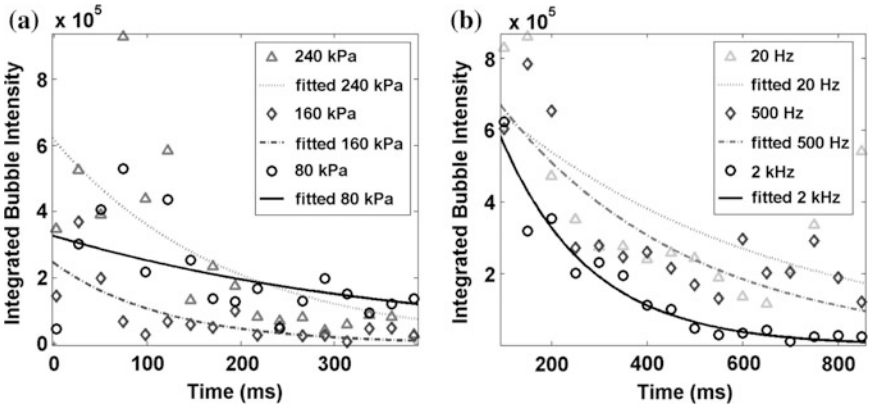

Fig. 2.50 The dissipation curves of cavitation bubbles under different UACM parameters, where exponential decay fitting was used. **a** The PNPs of UACM are 240, 180, and 80 kPa, with the same frame rate of 500 Hz. **b** The frame rates of UACM are 20, 500, and 2 kHz, while the PNP is 240 kPa. Reproduced with permission from Hu et al. © Acoustical Society of America

By combining plane wave transmission with MV beamforming and CF weighting, the frame rate of plane wave MVCF-based UACM can be significantly improved. In addition, the SNR of this technique is almost the same as in B-mode ACM, while the resolution is even higher than produced by B-mode ACM. Moreover, at a low imaging PNP, the effects of UACM on bubble behavior are small and can be neglected (Hu et al. 2015). So, plane wave MVCF-based UACM is feasible for imaging cavitation bubbles with relatively high SNR and good spatial–temporal resolution, as well as minor effects on bubble behavior.

2.6.3.1 2D UACM in a Free Fields

UACM can be employed to map both spatial–temporal evolution and dissolution of a cavitation bubble cloud that is induced by HIFU in water. This was done in the following experiments, where the electrical power was adjusted to 100 W, corresponding to a calculated total in situ spatial average intensity of about 2200 W/cm^2 (defined as I_{SAL}).

The spatial distributions of cavitation bubbles generated by a single HIFU pulse at different pulse durations are shown in Fig. 2.51. The cavitation bubbles first emerged in the focal region at a pulse duration of 50 μs, and then when the pulse duration increased, they grew and expanded forward into the post-focal region, finally appearing in the prefocal region. These results are consistent with previous studies that employed high-speed photography (Chen et al. 2006b) and a modified line-by-line scanning method (Sect. 2.5) (Ding et al. 2013).

Images of the evolution of a cavitation bubble cloud under successive HIFU pulses in a free field are shown in Fig. 2.52. Here, the duty cycle was 0.5 % and the

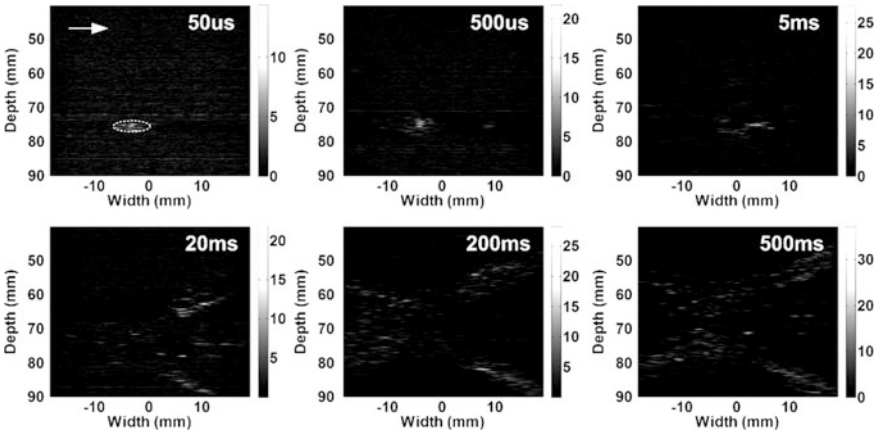

Fig. 2.51 Spatial distribution of cavitation bubbles generated by a single HIFU pulse at pulse durations varying from 50 μs to 500 ms in a free field. The *arrow* in the first image indicates the HIFU transmission direction

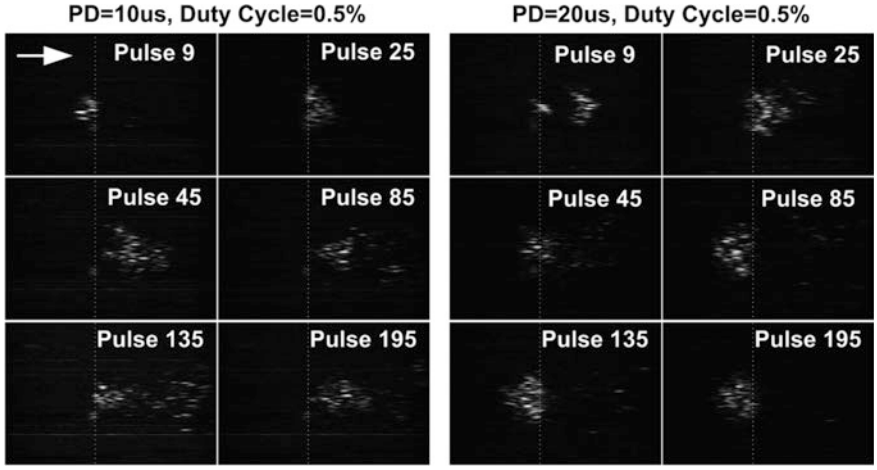

Fig. 2.52 UACM growth images of cavitation bubbles generated by successive HIFU pulses at a duty cycle of 0.5 % and pulse durations of 10 μs (*left*) and 20 μs (*right*) in a free field. The *arrow* in the first image indicates the HIFU transmission direction, and the *dotted line* indicates the center of the HIFU transducer's focal region

pulse duration was 10 and 20 μs. The bubble clouds were observed to grow and expand in the opposite direction for different pulse durations. For shorter pulses, the bubbles expanded away from the HIFU transducer because of the acoustic radiation force from HIFU. For longer pulses however, the bubbles expanded toward the HIFU transducer because enough bubbles were generated to cause acoustic "shadowing," which blocks the transmission of HIFU.

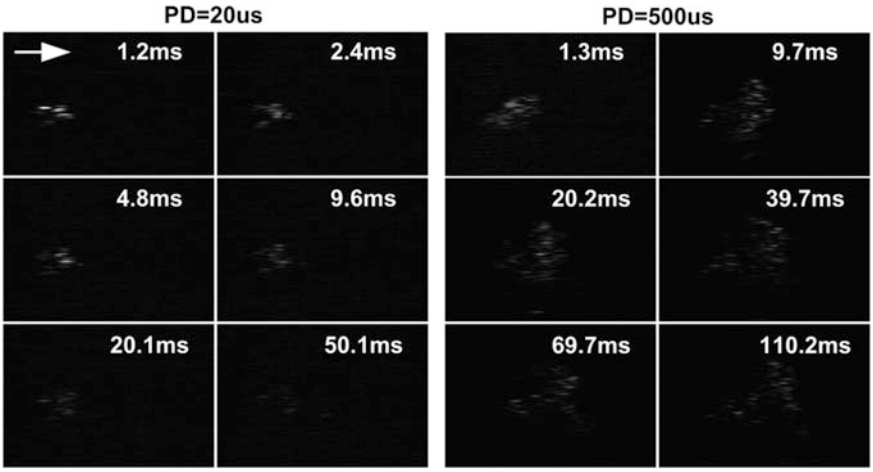

Fig. 2.53 UACM dissipation images of cavitation bubbles generated by a single HIFU pulse at pulse durations of 20 μs (*left*) and 500 μs (*right*) in a free field. The *arrow* in the first image indicates the HIFU transmission direction

Images showing the dissipation of cavitation bubbles can also be observed with UACM, as shown in Fig. 2.53, where cavitation bubbles were generated by a single HIFU pulse at different pulse durations in a free field. The results show that the overall size as well as the dissipation time of the cavitation bubble cloud increases with increasing pulse duration. The bubble cloud was almost disappeared after 50.1 ms for a pulse duration of 20 μs, while for a pulse duration of 500 μs, residual bubbles still remained after 110.2 ms.

2.6.3.2 3D Plane-by-Plane Cavitation Mapping

While UACM and PCM have been rapidly developed for cavitation detection by incorporating an array transducer to expand their spatial detection coverage for cavitation, these techniques only provide 2D cavitation maps, which give information about cavitation activity in only one plane. However, cavitation bubbles are produced in a 3D spatial area, which means that a 3D cavitation map is necessary for providing more complete information about cavitation activity.

A 3D plane-by-plane cavitation mapping technique based on the linear array of a current ultrasound diagnosis system has been proposed by Ding et al. (2013). With this technique, a cavitation event is mapped by a linear array of the ultrasound imaging system in plane wave transmitting and receiving mode, and then to extend this, a series of planes are sequentially measured, whereby these planes consist of the linear array positioned at different unit positions perpendicular to the axis of the HIFU transducer. Between two adjacent unit positions, there is a waiting time to allow the cavitation nuclei to distribute within the liquid such that it can return to its

original state. With this spatial series of channel-domain raw RF data, a 3D cavitation image can be formed that encompasses the entire cavitation volume detected at one time. To do this, the acquisition of the raw RF signals for each unit position is synchronized with the HIFU exposure. The duration of HIFU exposure, as well as the delay of the interrogating pulse relative to the moment when HIFU is turned off, can vary from microseconds to seconds. In addition, while experiments by Ding et al. (2013) produced a temporal resolution of several microseconds, this can be adjusted through hardware controls to reach submicrosecond-level resolution.

To map cavitation bubbles with a high spatial–temporal resolution and a high SNR, MV adaptive beamforming and CF weighting are used to process the raw RF data. In order to retain the quality of adaptive beamforming but to reduce the amount of data needed for calculations, MV beamforming processing is performed only on random resampling points from a certain bandwidth rather than on every sampling point. Next, the total information in the frequency domain is reconstructed by compressive sensing (CS), which effectively reduces the volume of the data involved in the beamforming calculation and significantly increases the rendering speed. After acquiring each output of beamformed RF data in 3D space, the 3D cavitation map can be reconstructed using the 3D reconstruction algorithm.

This ultrasound plane-by-plane 3D mapping is only valid when the cavitation distribution is repeatable when all conditions, including the HIFU output and the physical properties of the surrounding medium, are same. However, cavitation clouds will not likely be perfectly reproduced. Even so, Ding et al. (2013) showed that when specific test cases were examined multiple times, the method is repeatable on a broad scale of cavitation mapping. In their studies, a 5-MHz linear array (L14-5/38, Ultrasonix, Richmond, Canada) aligned parallel to the axis of an HIFU transducer (1.2 MHz, focal width 1.6 mm, focal length 8 mm, and aperture diameter 15 cm; Imasonic, Besancon, France) was used to detect the cavitation bubble population immediately after one HIFU exposure in plane wave transmitting and receiving mode (Sonix DAQ, Ultrasonix, Richmond, Canada). Using a three-axis stepper motor controller (Zolix SC300-3B, Beijing, China), the linear array was

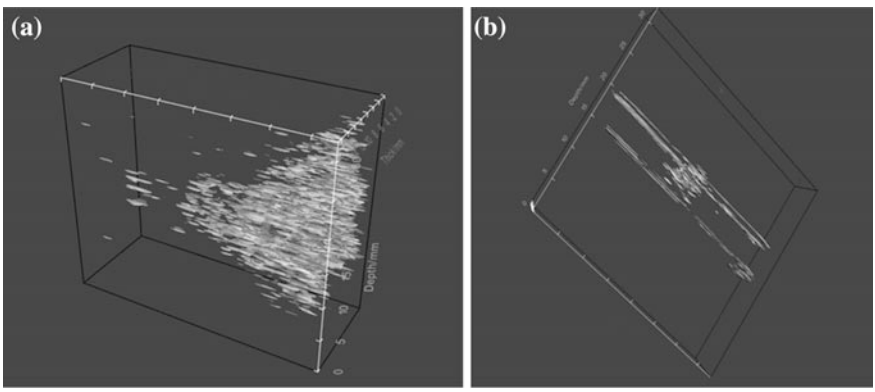

Fig. 2.54 Three-dimensional (3D) cavitation mapping **a** in tap water with a pulse duration of 20 ms and **b** in a phantom vessel with pulsatile flow and a pulse duration of 20 μs

positioned at each unit position perpendicular to the axis of HIFU transducer. This ultrasound plane-by-plane 3D cavitation mapping method was used to acquire the 3D spatial–temporal cavitation distribution in tap water and in a phantom vessel with pulsatile flow. As seen from the results in Fig. 2.54, the cavitation activity in 3D space was observed. Furthermore, the SNR of plane wave MVCF-based UACM was 20.45 ± 2.33 dB, which was almost same as that achieved in B-mode ACM. To quantify the improvement in resolution due to the beamforming, the −6 dB autocorrelation lengths of the enveloped RF data corresponding to the images were calculated. The resolution gain was defined as the ratio of the −6 dB autocorrelation lengths of the RF data before beamforming to those after beamforming. The lateral and axial resolution of plane wave MVCF-based UACM turned out to be 1.69 ± 0.12× and 2.33 ± 0.69× higher, respectively, than those resolutions in B-mode ACM.

2.7 Passive Cavitation Mapping

High-speed photography and the use of PCD have substantially improved our understanding of dynamic cavitation and its affiliated biological effects. Although PCD can resolve spatial sensitivity when receiving scattered signals, initial PCD strategies cannot distinguish individual bubbles in the cavitation bubble cloud because they rely on a single-element transducer. However, using a diagnostic ultrasound system with a linear array to map cavitation can allow us to identify cavitation along the transverse dire better axial resolution (Gyöngy and Coussios 2010a). The use of multi-element arrays as passive receivers can potentially provide substantial spatial information, thereby improving spatial and temporal resolution (Salgaonkar et al. 2009a). Therefore, PCM has been recently applied for this purpose, and it demonstrates very promising results for a wide range of applications, such for predicting and suppressing HIFU-induced vessel rupture (Hoerig et al. 2014), monitoring drug delivery (Nguyen et al. 2014), and transcranial mapping of diverging pressure waves (Arvanitis et al. 2014), to name a few.

In order to visualize the distribution of a cavitation bubble cloud produced after insonation with HIFU, post-beamforming of the spatial information is necessary. Several groups have approached this by performing passive beamforming in the time domain, which directly utilizes the cavitation recording acquired by the data acquisition board (Gyöngy and Coussios 2010a). In addition, cavitational features can also be characterized by transforming cavitation signals from the time domain to the Fourier domain (Salgaonkar et al. 2009a). In the following sections, we examine cavitation mapping from the perspectives of the time domain and the Fourier domain.

2.7.1 Time-Domain PCM

A signal of vibration or collapse from a single bubble can be considered as an emission from a cavitating point source. Therefore, a source field term s can be added that varies with position r and time t (Gyöngy et al. 2008):

$$\nabla^2 \mathrm{p} - \frac{1}{c}\frac{\partial^2 p}{\partial t^2} = -s(r,t) \tag{2.11}$$

where $s(r,t)$ represents the acoustic emissions arising from cavitation. This relationship represents the acoustic energy converted from the primary HIFU signal to broadband emissions, which is an indicator of inertial cavitation and gives the rate of the change in mass flow out of a unit volume. Integrating this source field over a volume V will yield the rate of change of mass flow out of that volume. According to the wave propagation, acoustic pressure can be depicted as follows:

$$p(r,t) = \int_v \frac{1}{4\pi|r-r'|} s(r', t-|r-r'|/c)dr' \tag{2.12}$$

One goal for cavitation maps is that they must directly correspond to the distribution of tissue damage that can be achieved by beamforming (DAS, for instance) the signals of array elements and then calculating the corresponding energy in time. Assuming that a linear array with elements at $(x_i, 0, 0)$ and focused in an $x-z$ plane, the source intensity map $S(x,z)$ for a time interval $[t_0, t_0+T]$ should be given as follows (Kennedy 2005):

$$S(x,z) = \frac{1}{T}\int_{t_o}^{t_0+T} \left(\sum_i H_i(x,z,t)\right)^2 \mathrm{d}t \tag{2.13}$$

where $H_i(x,z,t)$ is the back-propagated signal:

$$H_i(x,z,t) = \alpha(d_i(x,z))p_i(t + d_i(x,z)/c) \tag{2.14}$$

Here, $p_i(t)$ is the pressure sensed by array element i at time t, c is the speed of sound, and d_i is the propagation distance from point (x,z) to array element i:

$$d_i(x,z) = \sqrt{z^2 + (x_i - x)^2} \tag{2.15}$$

$\alpha(d_i)$ is the receiver spatial sensitive compensation term. Considering 2D spreading where the linear array is focused in a plane, $\alpha(d_i)$ can be chosen as $\alpha(d_i) = \sqrt{d_i}$.

Interestingly, B-mode imaging with the use of traditional receive-only arrays and the dynamic beamforming method has been shown to be similar to passive seismic

imaging achieved by time-exposure acoustics (TEA) (Kennedy 2005).The difference between them is that TEA effectively integrates the beamformed signal power over a time T, while B-mode imaging can only afford the envelope of the echo at a given time. Another distinguishing feature of TEA is that the axial resolution depends heavily on the receiving aperture, which is the same situation for passive beamforming. By contrast, the axial resolution of active B-mode ultrasound images is largely dependent on the transmitted pulse. Consequently, the receiving aperture may be varied with depth, which is called dynamic receive apodization.

Suppose a cavitation source $s(x, z, t)$ will generate the pressure filed $p(x, z, t)$. In order to estimate the source intensity S at position (x, z), we should calculate the back-propagating RF data from the signal on each receiving element to obtain the source intensity:

$$S(x,z) = \frac{1}{T}\int_0^{\mathrm{T}} \left\{ \left[\sum_{i=1}^{128} F_i(\tau) \right]^2 - \sum_{i=1}^{128} F_i(\tau)^2 \right\} \mathrm{d}t \tag{2.16}$$

where $F_i(\tau) = l_i * p_i(t - d_i/c + \tau)$ depicts the back-propagating signal. The term l_i represents the distance from point (x, z) to the array elements as follows:

$$l_i = \sqrt{z_s^2 + (x - x_s)^2} \tag{2.17}$$

Also, noting that:

$$\left(\sum_{i=1}^{128} k_i \right)^2 - \sum_{i=1}^{128} k_i^2 = 2 \sum_{\substack{i<j \\ i,j=1}}^{128} k_i k_j \tag{2.18}$$

we can change the integral order to obtain the cavitation source intensity:

$$S(x,z) = \sum_{\substack{i<j \\ i,j=1}}^{128} \left[\frac{2}{T} \int_0^T F_i(\tau) F_j(\tau) d\tau \right] \tag{2.19}$$

In addition, the axial resolution of passive cavitation maps created by a receive-only array would be degraded gradually as the distribution of the initial cavitation is extended along the axis of the HIFU transducer.

PCM, as mentioned above, is often produced by applying a passive beamforming algorithm for each location of interest. The recordings are appropriately delayed and summed together, with the mean square of the resulting signal providing a measure of the power emitted (Gyöngy and Coussios 2010b). However, passive beamfoming algorithms are unable to overcome the limit of Rayleigh

resolution (Gyöngy and Coviello 2011), and the quality of passive maps degrades when coherent sources interfere with each other (Gyöngy 2010).

Thus, producing high-resolution cavitation maps for coherent sources may rely on adaptive beamforming methods. For example, parametric techniques that are based on the separation of subspaces between the signal and the noise are one important class of approaches for improving the resolution of cavitation maps. However, these parametric techniques require that bubble sources must be considered as points, so they would not be useful in cases where the number of cavitation sources is unknown (Gyöngy and Coviello 2011).

Gyöngy and Coussios (2010a) proposed an effective method of mapping cavitation by using a linear array to receive emissions from cavitation bubbles. PCM can conveniently provide quantitative analysis of the source power and the change rate of source intensity. An appropriate system to study cavitation allows transmitters and receivers to be positioned at any angle, and the axis of HIFU transducer should be perpendicular to the receiver of diagnostic device. Figure 2.55 shows the resulting passive cavitation maps that describe three cavitation clusters during 1.06-MHz HIFU exposures. The change of source strength with time is also shown in this figure. The source power and the source intensity at a peak rarefactional focal pressure (PRFP) of 1.6 MPa are shown on the left and right, respectively. The right part of the figure illustrates the PCD signals of a single element, which shows that the bubble clusters near the HIFU source underwent cavitation every 3 cycles, while those farther away underwent cavitation every 2 cycles. Due to the signal attenuation and the signal bandwidth, the measurements of acoustic intensity and power were lower than their actual values. Also, the low lateral resolution of the mapping system may have been caused by a collection of massive microbubbles, and more detailed behavior of the bubbles should have been deduced by other information, such as periodic collapses.

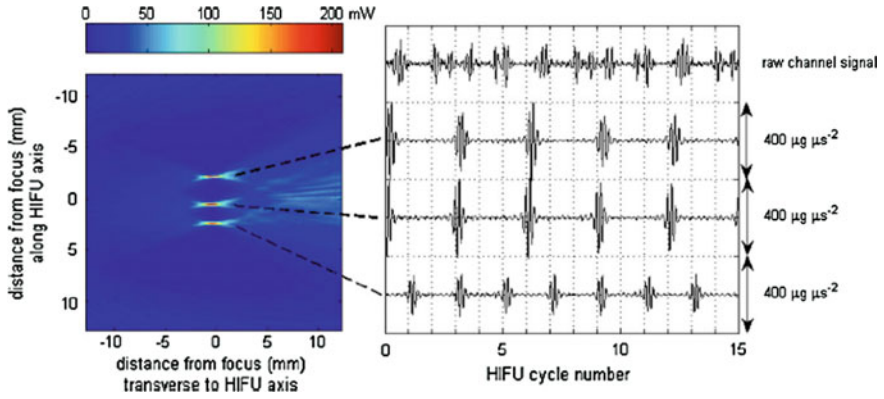

Fig. 2.55 Passive source power map (*left*) and source strengths (*right*) generated from the first frame recorded after HIFU was turned on, at a setting of 1.6 MPa PRFP. Reproduced with permission from Coussions et al. © Acoustical Society of America

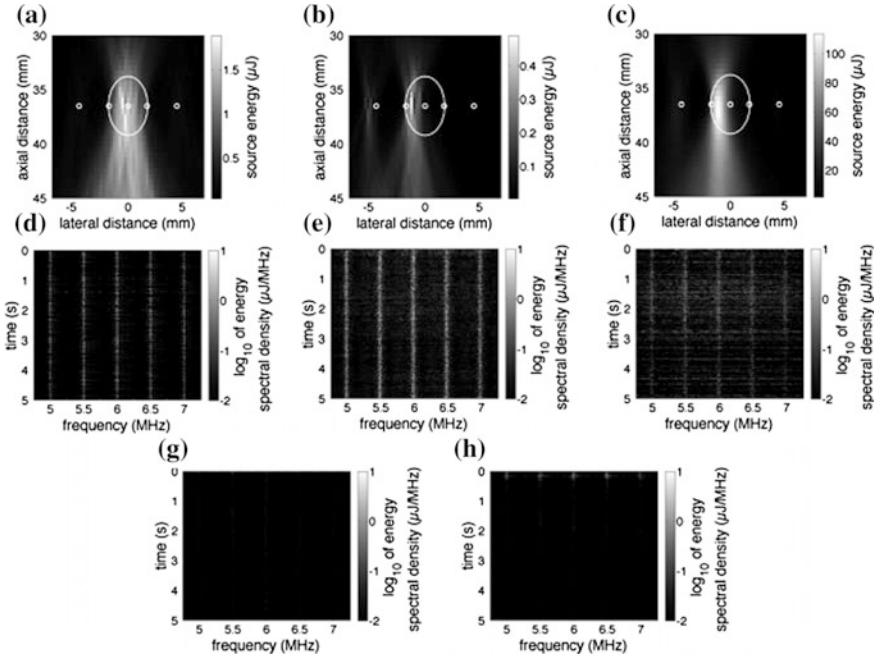

Fig. 2.56 PCI of single pulses and the accumulated total of all pulses, and the joint time–frequency-domain analyses of several points of interest labeled with little annulus in (**a**–**c**). Microbubbles were situated in 450 kPa PRPF, 50 Hz PRF, and 10 mm/s flow velocity. Large annulus in (**a**–**c**) indicates the focus region of focused ultrasound. Reproduced with permission from J.J. Choi et al. © Acoustical Society of America

Choi and Coussions (2012) also proposed a flow model to investigate spatial–temporal cavitation activity under disparate parameters by using passive acoustic imaging method in the time domain. They also combined a joint time–frequency-domain analysis with PCI to give information about the location of cavitation. Overall, this method was used to clarify the dynamic processes of focused ultrasound-induced cavitation in a flowing state. Figure 2.56a–c corresponds to images of the first pulse, final pulse, and the accumulated total of all 25 pulses, while figures (d–h) show the joint time–frequency-domain analyses of five points of interest. The main differences between the first and last pulse are embodied in the drastic decrease of the source energy at the focus and the attenuation of downstream microbubbles, which also can be observed in the total accumulated image. The strong broadband noise and strong harmonic components are clearly viewed in (e, f), both of which are contained within focal ROI and represent upstream microbubbles. And yet, downstream microbubbles, which are characterized by (g, h), seemed to produce few broadband recordings.

This technique allows us to adjust the position of HIFU relative to the linear array in order to investigate cavitation in the more complicated situation where the transmitting and receiving systems are separated; thus, this system provides much

more convenience and flexibility for experiments or applications. Even though it is hard to confirm the focal position very precisely, this system affords a possible approach to continuously monitor cavitation during the whole procedure of HIFU exposure. And thus, it can allow cavitation to be monitored in opaque tissues in real time.

Furthermore, Gyöngy and Coussions (2010b) implemented another design whereby the linear array was inserted into the middle of the HIFU, such that the imaging plane is parallel to the axial direction of the HIFU transducer. The position of the HIFU and linear array receiver were relatively fixed (Fig. 2.57) in this situation. This novel system employs a circular hole whose diameter equals the size of the linear array, whereby the linear array can rotate along an arbitrary direction. Thus, it can detect cavitation from every angle, providing more information about the distribution of microbubbles. Such a system has many possible uses in clinical applications.

Figure 2.58 shows localization of several cavitation sources by the PCI algorithm (Jensen et al. 2013). Because passive beamformed map of original data shown in Fig. 2.58a includes non-cavitational components, data should be filtered harmonic frequency components to reserve broadband noise, then spatial distribution map of cavitation can be obtained, as shown in Fig. 2.58b. Compared with Fig. 2.58b, c allows explicitly observing number and size of cavitation source through extracting outline of the former, and this method can effectively avoid interference and imaging artefacts in the maps.

Compared with conventional B-mode imaging, passive methods have excellent SNR because bright regions in PCM images are only caused acoustically by active bubbles and there is no speckle. Also, detection of cavitation by using this technique is more sensitive (Gyöngy and Coussios 2010b).

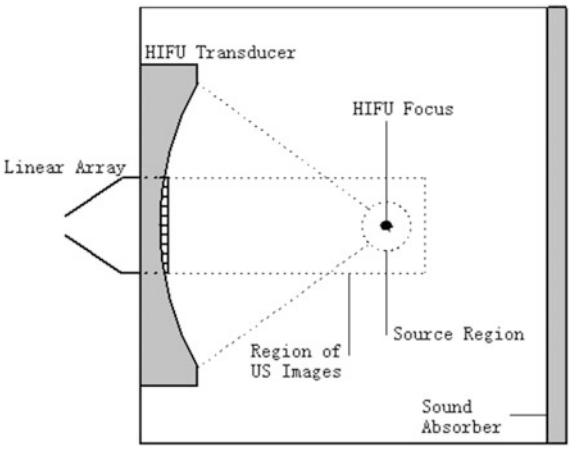

Fig. 2.57 Coaxial placement of an HIFU transducer and a linear array for PCM. Linear array is fixed in the middle of HIFU transducer and can passively receive emissions emanating from bubbles. The imaging plane is parallel to the axis of the HIFU transducer

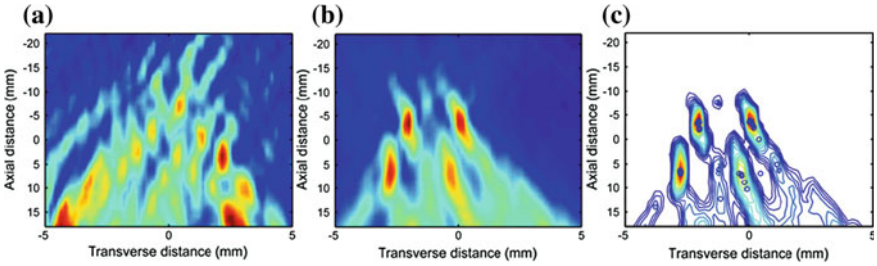

Fig. 2.58 Passive image of original data, passive image of data that has been filtered harmonic components, and contour map of filtered data. Reproduced with permission from C.R. Jensen et al. © 2013 IOP Publishing

Although broadband electrical noise may influence the detection of cavitation, distinction in the harmonics can be used to map cavitation. This allows us to localize the focus of low-intensity HIFU, which can injure biological tissue, and create 3D maps of cavitation to provide real-time feedback (Collin et al. 2013).

2.7.2 *Fourier-Domain PCM*

Salgaonkar (2009a) investigated passive cavitation maps from another distinct perspective, whereby the source intensity was characterized in the Fourier domain. The theory, which is called analytic expression, is similar to the theory of cavitation mapping based on DAS. The difference is that in the Fourier-domain theory, the signal should be processed in the frequency domain to portray its features. This is in direct contrast to the typical methods where signals are processed in the time domain (discussed above).

Specifically, as mentioned before, the pressure field at a position r for the point source radiating in a medium with density ρ and sound speed c is given by Blackstock (2000):

$$p(r,t) = \frac{\rho Q(t - |r|/c)}{4\pi|r|} \tag{2.20}$$

where $Q(t)$ is the volume flow of fluid from the source. Then, the received emission signal $s_n(t)$ for an element n centered at r_0 (region S_0) from a bubble at r_s is obtained by integrating the radiated pressure over the element surface. This can be finally expressed by the Rayleigh–Sommerfeld integral (Salgaonkar et al. 2009a):

$$s_n(t) = \int \frac{\rho Q(t - |r_0 - r_s|/c)}{4\pi|r_0 - r_s|} \mathrm{d}S_0 \tag{2.21}$$

which can be transformed into the frequency domain as:

$$S_m(\omega) = \frac{-i\omega\rho Q(\omega)}{4\pi} \int \frac{\exp(i|r_0 - r_s|\omega/c)}{|r_0 - r_s|} \mathrm{d}S_0 \tag{2.22}$$

where ω denotes radial frequency and $\mathrm{d}S_0$ is an area element on the receiver surface.

In order to produce passive cavitation maps, the brightness value for a passive image point (Y, Z) is defined as the total beamformed energy from a group of acoustic sources sensed by a transducer which is focused at that point:

$$I(Y, Z) = \sum_{\forall\omega} |S(\omega, Y, Z)|^2 \tag{2.23}$$

where ω is the radial frequency of a signal radiation frequency component and the symbol $\forall$ denotes summation over all radiating frequencies. When focusing an array with N elements on its axis at depth Z, the time delay applied to the nth element is expressed as:

$$\tau_n = \frac{-Z - \sqrt{(y_n - Y)^2 + Z^2}}{c} \tag{2.24}$$

The beamformed emission signal, corresponding to an image brightness value, is expressed as:

$$I(\omega, Y, Z) = \sum_{\forall\omega} \left| \sum_{\forall n} e^{j\omega T_n} S_n(\omega) \right|^2 \tag{2.25}$$

Salgaonkar et al. (2009a) designed a plan for evaluating signals in the Fourier domain (analytic expression) of PCM. In this setup (Fig. 2.59), the green rectangular box represents the linear array, while the gray cylinder represents the continuous-wave (CW) source. The orange test tube shape represents samples that are fixed in the middle. In their study, a 1-mm steel wire, a phosphate-buffered saline (PBS) solution, and a bovine liver were sonicated by CW ultrasound.

After sonicating PBS solution at 520 kHz with a PNP of 0.137 MPa, a constant 64-element subaperture (total 192 elements) was used to generate passive images from the ultraharmonic and broadband frequency components (Fig. 2.60). The cavitation cloud is clearly mapped (left image) in B-scan mode, and the result shows that the azimuth angle of the bubble clusters corresponds with the region where bubbles acted most dynamically. The center image was formed from the ultraharmonic emissions (6.5 MHz, or 12.5 × 520 kHz), while the right image was formed from the broadband emissions (6.3–6.7 MHz).

Processing signals in the frequency domain is based on the analytic expression, which was derived by numerically solving the Rayleigh–Sommerfeld integral under

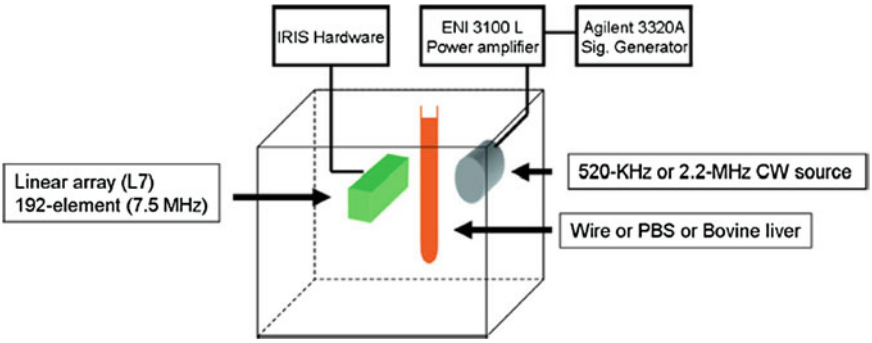

Fig. 2.59 Experimental setup for analytical expression in the frequency domain. Reproduced with permission from Salgaonkar et al. © Acoustical Society of America

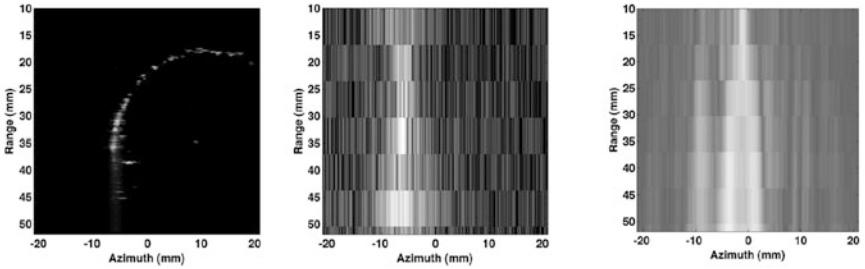

Fig. 2.60 Representative passive cavitation mapping in a saline solution for sonication at 520 kHz with 0.137 MPa peak negative pressure. Reproduced with permission from Salgaonkar et al. © Acoustical Society of America

the Fresnel approximation (Salgaonkar et al. 2009b). The results substantiate that passively receiving acoustic emissions can separate images for different frequency ranges. Consequently, this method provides a better way for focusing on information related to the frequency of interest. However, the B-scan mode does not have the capacity to distinguish the change in the size and position of cavitation events. In addition, this method allows cavitation sources to be localized more accurately in the array direction than in the range direction.

PCM may be the most effective way to monitor ultrasound ablation, because it has high sensitivity and a very high SNR compared with conventional B-mode images. Furthermore, this technique can provide higher frame frequency than MRI-guided imaging techniques. However, PCM cannot yet satisfactorily distinguish the distribution of a cavitation bubble cloud, mostly because of tissue heterogeneity and nonlinearity, especially in biological tissues. There are two possible ways to address this problem: increasing the array aperture and increasing the source frequency. In addition, a more complicated and effective imaging algorithm must be introduced for mapping and locating cavitation, thereby providing more

information for clinical applications. But, the complexity of the imaging algorithm must not impede the imaging speed of PCM. Further investigations should be focused on maintaining imaging speed while improving the resolution of passive maps.

2.8 Summary

In this chapter, cavitation detection and mapping techniques in water, including traditional methods and the latest developments, have been introduced. These methods provide technical support in cavitation research and can be improved for cavitation imaging in tissue, as cavitation mapping in water underpins how cavitation is studied in tissues. High-speed photography can be used to capture images of bubble dynamics and of the spatial–temporal distribution of the bubble cloud when ultrasound exposure is on. Also, SL and SCL provide more information about the spatial distribution of chemically active cavitation bubbles. However, these optical methods can only be employed in transparent media. PCD and PCM are performed by passively recording acoustic emissions from cavitation bubbles and thus can be employed to monitor cavitation activity during ultrasound exposure. Conversely ACD and ACM, which are based on pulse-echo mode, can only be used when ultrasound exposure is turned off, ensuring that they avoid interfering with the interrogating pulse.

Because acoustic cavitation is an evolutionary process, generally starting with the nucleation of a single bubble and often culminating with the formation of a bubble cloud, detecting and mapping methods fall into two classes: single-bubble detection and bubble cloud detection. Single-bubble dynamics may be studied by high-speed photography, SL and ACD. Lauterborn et al. investigated single-bubble dynamics with laser-produced bubbles and high-speed photography using framing rates up to 20.8 million fps. Single-bubble SL occurs when an acoustically trapped and periodically driven gas bubble collapses so strongly that the energy focusing at collapse leads to light emission. Additionally, ACD with high-frequency and narrowband transmitting pulses has been introduced for transient microcavitation detection, and it affords sufficient sensitivity and temporal resolution to noninvasively detect a single bubble of 1 μm. Also, the frequency shift signal obtained by the Doppler method is much higher than the signal caused by translation motion of a solid particle, so the rapid bubble growth and collapse characteristic of cavitation events can be distinguished via Doppler methods.

When a bubble cloud, rather than an individual bubble, has formed, a detectable amount of generated light or scattered acoustic emission may be produced, and thus, the limitations of the detector sensitivity can be solved. SL and SCL can be employed to map chemically active cavitation bubbles. However, the most common detection method to use with ultrasound exposure is PCD of the acoustic emissions generated by bubbles. Subharmonic and ultraharmonic emissions of the main excitation frequency can be used to reflect stable cavitation, while the broadband

noise emissions appearing above the background noise level indicate the presence of inertial cavitation. Also, the ICD and SCD can be calculated to reflect the relative intensity of inertial and stable cavitation. In order to increase the coverage of ACD and PCD, ACM and PCM have been developed by using a linear array connected to the ultrasound system in pulse-echo and "receive-only" mode, respectively. Here, we can achieve precise ACM by a modified ultrasound line-by-line scanning, and ultrafast ACM with plane wave beam. Although precise ACM is time consuming and can limited to a medium that offers a repeatable cavitation distribution, it can give good details with high sensitivity and spatial–temporal resolution, and it may develop as a standard cavitation mapping technique. Another technique, MVCF-based UACM, can map transient bubble clouds with relatively high SNR and good spatial–temporal resolution by combining plane wave transmission, MV beamforming, and CF weighting. Finally, using a passive beamforming algorithm on PCM data simultaneously acquired from all receiver elements of the linear array, it is feasible to map cavitation activity with time, supplying real-time cavitation maps during ultrasound treatment.

References

Abeyratne UR, Petropulu AP, Reid JM. Higher-order spectra based deconvolution of ultrasound images. IEEE Trans Ultrason Ferroelectr Freq Control. 1995;42:1064–75.

Akhatov I, Lindau O, Topolnikov A, Mettin R, Vakhitova N, Lauterborn W. Collapse and rebound of a laser-induced cavitation bubble. Phys Fluids. 2001;13:2805–19.

Ammi AY, Cleveland RO, Mamou J, Wang GI, Bridal SL, O'Brien WD. Ultrasonic contrast agent shell rupture detected by inertial cavitation and rebound signals. IEEE Trans Ultrason Ferroelectr Freq Control. 2006;53:126–36.

Apfel R. Acoustic cavitation inception. Ultrasonics. 1984;22:167–73.

Asl BM, Mahloojifar A. Minimum variance beamforming combined with adaptive coherence weighting applied to medical ultrasound imaging. IEEE Trans Ultrason Ferroelectr Freq Control. 2009;56:1923–31.

Arvanitis CD, Clement G, McDannold N. Transcranial passive cavitation mapping with a linear array: a simulation study with clinical datasets. J Acoust Soc Am. 2014;135:2210.

Atchley A, Frizzell L, Apfel R, Holland C, Madanshetty S, Roy R. Thresholds for cavitation produced in water by pulsed ultrasound. Ultrasonics. 1988;26:280–5.

Barnett S. Nonthermal issues: cavitation– its nature, detection and measurement. Ultrasound Med Biol. 1998;24:S11–21.

Blackstock DT. Fundamentals of physical acoustics. New York: Wiley; 2000.

Brenner MP, Hilgenfeldt S, Lohse D. Single-bubble sonoluminescence. Rev Mod Phys. 2002;74:425–84.

Cao H, Wan MX, Qiao YZ, Zhang SY, Li RX. Spatial distribution of sonoluminescence and sonochemiluminescence generated by cavitation bubbles in 1.2 MHz focused ultrasound field. Ultrason Sonochem. 2012;19:257–63.

Cao H, Yin H, Qiao YZ, Zhang SY, Wan MX. Sonochemiluminescence observation and acoustic detection of cavitation induced by pulsed HIFU at a tissue–fluid interface. Ultrason Sonochem. 2013;20:1370–5.

Capon J. High-resolution frequency-wavenumber spectrum analysis. Proc IEEE. 1969;57:1408–18.

Chambers L. The emission of visible light from pure liquids during acoustic excitation. Phys Rev. 1936;49:881.
Chen H, Kreider W, Brayman AA, Bailey MR, Matula TJ. Blood vessel deformations on microsecond time scales by ultrasonic cavitation. Phys Rev Lett. 2011;106:034301.
Chen H, Li XJ, Wan MX. The inception of cavitation bubble clouds induced by high-intensity focused ultrasound. Ultrasonics. 2006a;44:e427–9.
Chen H, Li XJ, Wan MX. Spatial–temporal dynamics of cavitation bubble clouds in 1.2 MHz focused ultrasound field. Ultrason Sonochem. 2006b;13:480–6.
Chen H, Li XJ, Wan MX, Wang SP. High-speed observation of cavitation bubble clouds near a tissue boundary in high-intensity focused ultrasound fields. Ultrasonics. 2009;49:289–92.
Chen W-S, Brayman AA, Matula TJ, Crum LA. Inertial cavitation dose and hemolysis produced in vitro with or without Optison®. Ultrasound Med Biol. 2003a;29:725–37.
Chen W-S, Brayman AA, Matula TJ, Crum LA, Miller MW. The pulse length-dependence of inertial cavitation dose and hemolysis. Ultrasound Med Biol. 2003b;29:739–48.
Chen W-S, Matula TJ, Crum LA. The disappearance of ultrasound contrast bubbles: observations of bubble dissolution and cavitation nucleation. Ultrasound Med Biol. 2002;28:793–803.
Choi JJ, Coussios C-C. Spatiotemporal evolution of cavitation dynamics exhibited by flowing microbubbles during ultrasound exposure. J Acoust Soc Am. 2012;132:3538–49.
Chomas JE, Dayton P, May D, Ferrara K. Threshold of fragmentation for ultrasonic contrast agents. J Biomed Opt. 2001;6:141–50.
Cole RH. Underwater explosions. New York: Dover Publications; 1965.
Coleman AJ, Saunders JE, Crum LA, Dyson M. Acoustic cavitation generated by an extracorporeal shockwave lithotripter. Ultrasound Med Biol. 1987;13:69–76.
Collin J, Coviello C, Lyka E. Real-time three-dimensional passive cavitation detection for clinical high intensity focused ultrasound systems. J Acoust Soc Am. 2013;133:3263.
Cox H, Zeskind RM, Owen MM. Robust adaptive beamforming. IEEE Trans Acoust Speech Sign Process. 1987;35:1365–76.
Crum LA. Acoustic cavitation. In: Proceeding of 1982 IEEE ultrasonics symposium. New York: IEEE; 1982. pp 1–11.
Crum LA, Roy RA, Dinno MA, Church CC, Apfel RE, Holland CK, Madanshetty SI. Acoustic cavitation produced by microsecond pulses of ultrasound: a discussion of some selected results. J Acoust Soc Am. 1992;91:1113–9.
Deng CX, Xu Q, Apfel RE, Holland CK. In vitro measurements of inertial cavitation thresholds in human blood. Ultrasound Med Biol. 1996;22:939–48.
Ding T, Zhang SY, Fu QY, Xu ZA, Wan MX. Ultrasound line-by-line scanning method of spatial–temporal active cavitation mapping for high-intensity focused ultrasound. Ultrasonics. 2013;54:147–55.
Everbach EC, Francis CW. Cavitational mechanisms in ultrasound-accelerated thrombolysis at 1 MHz. Ultrasound Med Biol. 2000;26:1153–60.
Farny CH, Holt RG, Roy RA. Temporal and spatial detection of HIFU-induced inertial and hot-vapor cavitation with a diagnostic ultrasound system. Ultrasound Med Biol. 2009;35:603–15.
Fernandez Rivas D, Ashokkumar M, Leong T, Yasui K, Tuziuti T, Kentish S, Lohse D, Gardeniers HJ. Sonoluminescence and sonochemiluminescence from a microreactor. Ultrason Sonochem. 2012;19:1252–9.
Frenzel J, Schultes H. Zeit. für Physical Chemistry 1934;421.
Frommhold L. Electron-atom bremsstrahlung and the sonoluminescence of rare gas bubbles. Phys Rev E. 1998;58:1899–905.
Gaitan DF, Crum LA, Church CC, Roy RA. Sonoluminescence and bubble dynamics for a single, stable, cavitation bubble. J Acoust Soc Am. 1992;91:3166–83.
Gateau J, Aubry JF, Pernot M, Fink M, Tanter M. Combined passive detection and ultrafast active imaging of cavitation events induced by short pulses of high-intensity ultrasound. IEEE Trans Ultrason Ferroelectr Freq Control. 2011a;58:517–32.
Gateau J, Aubry JF, Chauvet D, Boch A, Fink M, Tanter M. In vivo bubble nucleation probability in sheep brain tissue. Phys Med Biol. 2011b;56:7001.

Greenspan HP, Nadim A. On sonoluminescence of an oscillating gas bubble. Phys Fluids A. 1993;5:1065–7.
Gyöngy M. Passive cavitation mapping for monitoring ultrasound therapy. Oxford: Oxford University; 2010.
Gyöngy M, Arora M, Noble JA, Coussios CC. Use of passive arrays for characterization and mapping of cavitation activity during HIFU exposure. In: Proceeding of 2008 IEEE ultrasonics symposium. Beijing: IEEE; 2008. pp. 871–74.
Gyöngy M, Coussios C-C. Passive cavitation mapping for localization and tracking of bubble dynamics. J Acoust Soc Am. 2010a;128:EL175–80.
Gyöngy M, Coussios C-C. Passive spatial mapping of inertial cavitation during HIFU exposure. IEEE Trans Biomed Eng. 2010;57:48–56.
Gyöngy M, Coviello CM. Passive cavitation mapping with temporal sparsity constraint. J Acoust Soc Am. 2011;130:3489–97.
Hallez L, Touyeras F, Hihn JY, Klima J, Guey JL, Spajer M, Bailly Y. Characterization of HIFU transducers designed for sonochemistry application: cavitation distribution and quantification. Ultrasonics. 2010;50:310–7.
Hammer D, Frommhold L. Electron-ion bremsstrahlung spectra calculations for sonoluminescence. Phys Rev E. 2002;66:056303.
Hatanaka S-I, Yasui K, Tuziuti T, Mitome H. Difference in threshold between sono-and sonochemical luminescence. Jpn J Appl Phys. 2000;39:2962–6.
Hoerig CL, Serrone JC, Burgess MT, Zuccarello M, Mast TD. Prediction and suppression of HIFU-induced vessel rupture using passive cavitation detection in an ex vivo model. J Ther Ultrasound. 2014;2:14.
Holland CK, Roy R, Apfel R, Crum L. In vitro detection of cavitation induced by a diagnostic ultrasound system. IEEE Trans Ultrason Ferroelectr Freq Control. 1992;39:95–101.
Hollman K, Rigby K, O'Donnell M. Coherence factor of speckle from a multi-row probe. In: Proceeding of 1999 IEEE ultrasonics symposium. Caesars Tahoe: IEEE; 1999. pp. 1257–1260.
Holt M. Underwater explosions. Annu Rev Fluid Mech. 1977;9:187–214.
Hu H, Xu SS, Yuan Y, Liu RN, Wang SP, Wan MX. Spatial–temporal ultrasound imaging of residual cavitation bubbles around a fluid-tissue interface in histotripsy. J Acoust Soc Am. 2015;137:2563–2572.
Jarman P. Sonoluminescence: a discussion. J Acoust Soc Am. 2005;32:1459–62.
Jensen CR, Cleveland RO, Coussios CC. Real-time temperature estimation and monitoring of HIFU ablation through a combined modeling and passive acoustic mapping approach. Phys Med Biol. 2013;58:5833–50.
Kennedy JE. High-intensity focused ultrasound in the treatment of solid tumours. Nat Rev Cancer. 2005;5:321–7.
Khokhlova T, Li T, Sapozhnikov O, Hwang JH. The use of twinkling artifact of Doppler imaging to monitor cavitation in tissue during high intensity focused ultrasound therapy. In: Proceedings of meetings on acoustics. Montreal: Acoustical Society of America; 2013. p. 075034.
Lauterborn W, Ohl C-D. Cavitation bubble dynamics. Ultrason Sonochem. 1997;4:65–75.
Leighton TG. The acoustic bubble. London: Academic Press; 1994.
Leighton TG, Walton A, Field J. High-speed photography of transient excitation. Ultrasonics. 1989;27:370–3.
Li T, Khokhlova T, Sapozhnikov O, O'Donnell M, Hwang JH. A new active cavitation mapping technique for pulsed HIFU applications-bubble doppler. IEEE Trans Ultrason Ferroelectr Freq Control. 2014;61:1698–708.
Luther S, Mettin R, Koch P, Lauterborn W. Observation of acoustic cavitation bubbles at 2250 frames per second. Ultrason Sonochem. 2001;8:159–62.
Mast TD, Salgaonkar VA, Karunakaran C, Besse JA, Datta S, Holland CK. Measurements of cavitation dose, echogenicity, and temperature during ultrasound ablation. In: 6th international symposium on therapeutic ultrasound. Oxford: AIP Conference Proceedings; 2007. pp. 335–41.

McLaughlan J, Rivens I, Haar GT, Shaw A, Leighton T, Humphrey V, Birkin P, Vian C. The design and implementation of a passive cavitation detection system for use with ex vivo tissue. In: 5th international symposium on therapeutic ultrasound. New York: AIP Conference Proceedings; 2006. pp. 338–42.

McLaughlan J, Rivens I, ter Haar G. Cavitation detection in ex vivo bovine liver tissue exposed to high intensity focused ultrasound (HIFU). In: 4th IEEE international symposium on biomedical imaging: from nano to macro. Arlington: IEEE; 2007. pp. 1124–27.

McLaughlan J, Rivens I, Leighton T, ter Haar G. A study of bubble activity generated in ex vivo tissue by high intensity focused ultrasound. Ultrasound Med Biol. 2010;36:1327–44.

McMurray H, Wilson B. Mechanistic and spatial study of ultrasonically induced luminol chemiluminescence. J Phys Chem A. 1999;103:3955–62.

Moss WC, Clarke DB, White JW, Young DA. Hydrodynamic simulations of bubble collapse and picosecond sonoluminescence. Phys Fluids. 1994;6:2979–85.

Moussatov A, Granger C, Dubus B. Cone-like bubble formation in ultrasonic cavitation field. Ultrason Sonochem. 2003;10:191–5.

Neppiras E, Noltingk B. Cavitation produced by ultrasonics: theoretical conditions for the onset of cavitation. Proc Phys Soc Sect B. 1951;64:1032–38.

Nguyen MM, Kopechek JA, Hasjim B, Villanueva FS, Kim K. Passive cavitation imaging with nucleic acid-loaded microbubbles in mouse tumors. J Acoust Soc Am. 2014;136:2302.

Noltingk BE, Neppiras EA Cavitation produced by ultrasonics. Proc Phys Soc Sect B. 1950;63:674–85.

Ohl S-W, Ow DS-W, Klaseboer E, Wong VV, Camattari A, Ohl C-D. Creation of cavitation activity in a microfluidic device through acoustically driven capillary waves. Lab Chip. 2010;10:1848–55.

Pecha R, Gompf B. Microimplosions: cavitation collapse and shock wave emission on a nanosecond time scale. Phys Rev Lett. 2000;84:1328–30.

Putterman S, Weninger K. Sonoluminescence: how bubbles turn sound into light. Annu Rev Fluid Mech. 2000;32:445–76.

Rabkin BA, Zderic V, Vaezy S. Hyperecho in ultrasound images of HIFU therapy: involvement of cavitation. Ultrasound Med Biol. 2005;31:947–56.

Robinson P, Blake J, Kodama T, Shima A, Tomita Y. Interaction of cavitation bubbles with a free surface. J Appl Phys. 2001;89:8225–37.

Roy RA, Madanshetty SI, Apfel RE. An acoustic backscattering technique for the detection of transient cavitation produced by microsecond pulses of ultrasound. J Acoust Soc Am. 1990;87:2451.

Salgaonkar VA, Datta S, Holland CK, Mast TD. Passive cavitation imaging with ultrasound arrays. J Acoust Soc Am. 2009a;126:3071–83.

Salgaonkar VA, Datta S, Holland CK, Mast TD. Passive imaging of cavitational acoustic emissions with ultrasound arrays. In: AIP conference proceedings, 2009b. pp. 73–7.

Shi WT, Forsberg F, Tornes A, Ostensen J, Goldberg B. Experimental investigation of contrast microbubble destruction. In: Proceeding of 2001 IEEE ultrasonics symposium, Atlanta: IEEE; 2001. pp. 1691–94.

Shi WT, Forsberg F, Tornes A, Ostensen J, Goldberg BB. Destruction of contrast microbubbles and the association with inertial cavitation. Ultrasound Med Biol. 2000;26:1009–19.

Suslick KS. Sonochemistry. Science. 1990;247:1439–45.

Suslick KS, Didenko Y, Fang MM, Hyeon T, Kolbeck KJ, McNamara WB, Mdleleni MM, Wong M. Acoustic cavitation and its chemical consequences. Philos Trans R Soc Lond Ser A Math Phys Eng Sci. 1999;357:335–53.

Suslick KS, Hammerton DA, Cline RE. Sonochemical hot spot. J Am Chem Soc. 1986;108:5641–2.

Synnevag JF, Austeng A, Holm S. Adaptive beamforming applied to medical ultrasound imaging. IEEE Trans Ultrason Ferroelectr Freq Control. 2007;54:1606–13.

Taylor K, Jarman P. The spectra of sonoluminescence. Aust J Phys. 1970;23:319–34.

Tu J, Matula TJ, Brayman AA, Crum LA. Inertial cavitation dose produced in *ex vivo* rabbit ear arteries with optison@ by 1-MHz pulsed ultrasound. Ultrasound Med Biol. 2006;32:281–8.

Vaezy S, Andrew M, Kaczkowski P, Crum L. Image-guided acoustic therapy. Annu Rev Biomed Eng. 2001a;3:375–90.

Vaezy S, Martin R, Mourad P, Crum L. Hemostasis using high intensity focused ultrasound. Eur J Ultrasound. 1999;9:79–87.

Vaezy S, Shi X, Martin RW, Chi E, Nelson PI, Bailey MR, Crum LA. Real-time visualization of high-intensity focused ultrasound treatment using ultrasound imaging. Ultrasound Med Biol. 2001b;27:33–42.

Vaezy S, Vaezy S, Starr F, Chi E, Cornejo C, Crum L, Martin RW. Intra-operative acoustic hemostasis of liver: production of a homogenate for effective treatment. Ultrasonics. 2005;43:265–9.

Vazquez G, Camara C, Putterman S, Weninger K. Sonoluminescence: nature's smallest blackbody. Opt Lett. 2001;26:575–7.

Wang ZS, Li J, Wu RB. Time-delay-and time-reversal-based robust Capon beamformers for ultrasound imaging. IEEE Trans Med Imaging. 2005;24:1308–22.

Xu N, Wang L, Hu XW. Numerical study of electronic impact and radiation in sonoluminescence. Phys Rev E. 1998;57:1615–20.

Xu N, Wang L, Hu XW. Extreme electrostatic phenomena in a single sonoluminescing bubble. Phys Rev Lett. 1999;83:2441.

Xu N, Wang L, Hu XW. Bremsstrahlung of nitrogen and noble gases in single-bubble sonoluminescence. Phys Rev E. 2000;61:2611–6.

Xu Z, Raghavan M, Hall TL, Mycek M-A, Fowlkes JB, Cain CA. Evolution of bubble clouds induced by pulsed cavitational ultrasound therapy-histotripsy. IEEE Trans Ultrason Ferroelectr Freq Control. 2008;55:1122–32.

Yasui K. Mechanism of single-bubble sonoluminescence. Phys Rev E. 1999;60:1754–8.

Young FR. Sonoluminescence. Boca Raton: CRC Press; 2004.

Zhang SY, Li C, Yin H, Wang SP, Wan MX. Surface vibration and nearby cavitation of an ex vivo bovine femur exposed to high intensity focused ultrasound. J Acoust Soc Am. 2013;134:1656–62.

http://www.springer.com/978-94-017-7254-9

Cavitation in Biomedicine
Principles and Techniques
Wan, M.; Feng, Y.; Haar, G.t. (Eds.)
2015, XVII, 503 p. 403 illus., 104 illus. in color.,
Hardcover
ISBN: 978-94-017-7254-9